Physics of Fluids

RESEARCH ARTICLE | OCTOBER 22 2026

Flow mechanism on the air–water mixed wakes of an air lubrication ship: A numerical study

Qidi Gao (高启迪) ; Xiaosong Zhang (张晓嵩); Decheng Wan (万德成) ; Jianhua Wang (王建华)

Check for updates

Physics of Fluids 38, 105174 (2026)
https://doi.org/10.1063/5.0353056

View Online Export Citation

Articles You May Be Interested In

Flame properties of auto-ignition assisted supersonic shear layer hydrogen flames
Physics of Fluids (September 2026)

Influences of herringbone riblets on shock-wave/turbulent boundary layer interactions in supersonic compression-ramp flow
Physics of Fluids (August 2025)

Vortex dynamics and hydrodynamic mechanisms of tandem flood holes on an underwater vehicle
Physics of Fluids (March 2026)

22 October 2026 13:43:54

AIP Publishing
Physics of Fluids
Special Topics Open for Submissions
Learn More

AIP Publishing

Physics of Fluids ARTICLE pubs.aip.org/aip/pof

Flow mechanism on the air–water mixed wakes of an air lubrication ship: A numerical study

Cite as: Phys. Fluids **38**, 105174 (2026); doi: 10.1063/5.0353056
Submitted: 19 July 2026 · Accepted: 9 October 2026 ·
Published Online: 22 October 2026

View Online Export Citation CrossMark

Qidi Gao (高启迪),[1] Xiaosong Zhang (张晓嵩),[2,3] Decheng Wan (万德成),[1] and Jianhua Wang (王建华)[1,a)]

AFFILIATIONS

[1]Computational Marine Hydrodynamic Lab (CMHL), School of Naval Architecture, Ocean and Civil Engineering, Shanghai Jiao Tong University, Shanghai 200240, China
[2]Shanghai Branch, China Ship Scientific Research Center, Shanghai 200011, China
[3]CSSC Shanghai Marine Energy Saving Technology Co., Ltd., Shanghai 200011, China

[a)]Author to whom correspondence should be addressed: jianhuawang@sjtu.edu.cn

ABSTRACT

Numerous studies have demonstrated the effectiveness of ship air-layer drag reduction (ALDR), as a form of ship air lubrication, in reducing frictional resistance. However, research on air distribution around the hull and the influence of air-entrained stern wakes on the wake field remains limited. In this paper, the Euler–Euler two-fluid method integrated with the interfacial area transport equation (IATE) in the open-source platform OpenFOAM is employed to investigate a specially designed oil tanker equipped with an air-layer device. The numerical method is validated by comparison with experimental wake results. The results show that the present method reproduces the mean wake fraction at the propeller disk plane with errors of 6.89% and −9.6% under single-phase and air-entrained conditions, respectively, and captures the main features of the air-entrained stern wake. The air layer beneath the hull exhibits a tendency of cyclic accumulation–instability–reaccumulation, as observed in the present simulations, with maximum thickness in the mid-ship region. At the stern, the air fraction decreases from 4.42% to 0.57% downstream, while the stern separation vortex retains a portion of microbubbles, carrying approximately 0.17% air fraction to the rearmost propeller plane station. After applying ALDR, the high wake fraction region is substantially reduced, and the mean wake fraction at the propeller disk decreases by about 49% compared with the single-phase case. Meanwhile, the streamline pattern transitions from a dual-vortex to a single-core vortex structure. These findings suggest that, within the present numerical framework, ALDR may modify the stern flow vorticity dynamics, providing preliminary insights into the air–water mixed wake characteristics. Quantitative drag reduction effects are not evaluated in this study.

Published under an exclusive license by AIP Publishing. https://doi.org/10.1063/5.0353056

22 October 2026 13:43:54

I. INTRODUCTION

In the field of naval architecture and ocean engineering, ship resistance has long been a key concern. The magnitude of resistance encountered by a ship during navigation directly affects fuel consumption and, consequently, the vessel's economic performance. Reducing ship resistance has become an effective approach to achieve energy savings and emission reduction. For ships engaged in shipping operations, frictional resistance constitutes a major component of total resistance, accounting for approximately 50%–60%.[1] Other components, such as pressure resistance, contribute only a small portion at lower speeds. Currently, most research on hull form optimization aims to reduce pressure resistance.[2] However, further performance improvements through this approach are approaching their limit, making further progress difficult. Therefore, new drag reduction technologies are urgently needed to enhance ship performance by reducing resistance.

Air lubrication drag reduction technology for ships has developed rapidly in recent years. Owing to its high drag reduction rate, low energy consumption, and environmental friendliness, it has emerged as an efficient drag reduction technology for ships.[3] Although the specific drag reduction mechanisms remain to be fully verified, generally recognized mechanisms include the surface slip phenomenon;[4] reduced effective viscosity in the boundary layer due to decreased mixture density in air–liquid flows;[5] and changes in local friction resistance caused by near-wall porosity variations in microbubble drag reduction.[6,7] Additionally, turbulence suppression plays a role: bubble coalescence, breakup, and streamwise shear deformation can reduce turbulence intensity in the boundary layer.[8] Gao *et al.*[9] conducted flat-plate experiments and found that bubble injection alters the flow characteristics of the plate boundary layer, reducing flow velocity and suppressing turbulence development, thereby decreasing surface friction resistance. Moreover, many studies have

Published under an exclusive license by AIP Publishing

demonstrated that if a continuous air layer can be formed to achieve air lubrication, the drag reduction effect is even greater. A continuous air layer can reduce surface friction resistance by approximately 80%.[10] Under air-layer drag reduction (ALDR) conditions, a stable air layer can even reduce cavity pressure resistance.[11] In summary, extensive existing research has confirmed the effectiveness of air lubrication technology, particularly ship air-layer drag reduction. However, studies on specific drag reduction mechanisms remain insufficient due to limitations in experimental and numerical models, which directly hinders practical engineering applications of this technology. Therefore, numerical simulation research on ship ALDR is both necessary and significant.

Computational fluid dynamics (CFD) has always played an important role in investigating flow mechanisms, especially in complex flows where experimental data are difficult to obtain. For ship ALDR, CFD has contributed substantial research and experience. For the air–liquid two-phase flow involved in ALDR, many numerical studies have made achievements in both methods and result analyses.[12–14] Current numerical simulations of two-phase flow typically establish mathematical models for bubbles and the continuous liquid phase separately. Methods for calculating the discrete phase (bubbles) can be classified into Euler–Euler and Euler–Lagrange approaches. Kunz *et al.*[15] performed numerical calculations on bubble drag reduction using the Eulerian two-phase flow model, explaining the detailed flow in the air-mixed boundary layer and the evolving behavior of bubbles, thereby demonstrating the feasibility of this method for bubble drag reduction problems. Hoang *et al.*[16] focused numerical studies of ship ALDR on the air morphology in the mixture and proposed a boundary-layer-specific calculation approach.

For more detailed bubble motion, the Euler–Lagrange method offers advantages. Although this method is mainly used in chemical engineering and other disciplines, it can effectively simulate bubble coalescence and breakup.[14,17] For bubble drag reduction, Zhang *et al.*[18] proposed a bubble coalescence and breakup model, combining the volume-of-fluid (VOF) method with Lagrangian tracking to identify coalescence and breakup events. This method can also calculate coalescence and breakup of bubble swarms in bubble drag reduction problems.[19] Although the Euler–Lagrange method has advantages in bubble drag reduction computations, it requires solving the motion of discrete microbubbles as individual particles, incurring high computational costs and thus being unsuitable for large-scale ship model simulations.

In contrast, the Euler–Euler method, which treats bubbles as a dispersed phase without solving individual bubble motion, is more appropriate for ship air lubrication drag reduction problems. However, to accurately describe the interaction between the dispersed phase and the liquid, various force models must be introduced, including bubble drag models such as the Schiller–Naumann model,[20] Ishii model,[21] and Tomiyama model,[22] as well as lift force model[22] and virtual mass force model.[23] Zhao and Zong[24] used the Euler–Euler method to study bubble drag reduction on a model-scale ship, considering bubble coalescence and breakup. Shao *et al.*[25] employed the Eulerian multiphase method to investigate microbubble drag reduction on an axisymmetric body, focusing on the effect of bubbles on pressure resistance. However, in their study, bubble diameter was set as constant, and bubble coalescence and breakup were neglected. Mohammadpour *et al.*[26] used the VOF method to study the effect of bubble drag reduction on full-scale ships at different drafts and obtained a maximum drag reduction of 10.45%. Zhao *et al.*[27] performed numerical simulations of microbubble drag reduction on a model-scale Korea Research Institute of Ships and Ocean Engineering (KRISO) Very Large Crude Carrier (KVLCC) hull using a two-fluid model, considering bubble coalescence and breakup. The study mainly discussed the influence of different bubble diameters on mixture flow and air distribution, concluding that bubbles can affect pressure resistance by changing the flow velocity at the stern, but no further analysis of the detailed mixture flow was provided.

In summary, research on ship ALDR remains very limited to date. Moreover, no universally applicable numerical simulation method exists for ship ALDR that can both capture the complex and fine flow characteristics of air–liquid mixtures and efficiently solve large-scale model problems. Furthermore, studies on the flow evolution of air–liquid mixtures beneath and behind the ship hull, air distribution, and the influence on the stern wake field are scarce. Since ALDR inevitably causes some air to flow into the propeller inflow field, resulting in an air-entrained propeller inflow,[28] the propeller efficiency is affected. Different air content levels can reduce propeller propulsion efficiency to varying degrees.[29] Therefore, the flow evolution of the air–liquid mixture around the ship with ALDR, the development of the mixture flow and air distribution at the stern, and the impact of the mixture on the nominal wake field are critically important. These issues affect ship propulsion performance and thus reduce the total drag reduction benefit of ALDR.

To address this problem, the present study adopts the Euler–Euler two-fluid method coupled with the interfacial area transport equation (IATE) as the numerical simulation approach, as this combination balances computational efficiency for large-scale ship models with the capability to account for bubble coalescence and breakup. Numerical simulations are performed on a specially designed model-scale KVLCC ship equipped with an ALDR device on the bottom. The primary objectives are threefold: first, to validate the proposed method against experimental wake data; second, to analyze the spatial distribution and thickness variation of the air layer beneath the hull; third, to investigate the dispersion patterns of air at the stern and the resulting modifications to the nominal wake field. This work is motivated by the fact that ALDR inevitably introduces air into the propeller inflow, which may degrade propulsion efficiency, making a thorough understanding of the air–water mixed flow and its wake impact critically important for practical ALDR applications. It should be noted that, unlike well-stratified two-phase flows, the numerical prediction of resistance for ship ALDR remains a challenging issue due to the complex and highly unsteady air–water interface and the associated modeling uncertainties. Therefore, the present study does not aim to quantify drag reduction or propulsion efficiency; rather, it focuses on the characterization of the air-layer evolution and the air-entrained wake modifications. Quantitative assessments of resistance and propulsion performance are left for future work.

II. NUMERICAL METHOD

A. Governing equations

In this paper, the Euler–Euler two-fluid method is used as the numerical approach to solve the air–water two-phase flow for ship ALDR, based on the incompressible Navier–Stokes equations. Water

22 October 2026 13:43:54

Published under an exclusive license by AIP Publishing

is treated as the continuous phase, and air as the discrete phase. The governing equations are expressed as

$$\frac{\partial(\alpha_\varphi \rho_\varphi)}{\partial t} + \nabla \cdot (\alpha_\varphi \rho_\varphi \boldsymbol{U}_\varphi) = 0, \tag{1}$$

$$\frac{\partial(\alpha_\varphi \rho_\varphi \boldsymbol{U}_\varphi)}{\partial t} + \nabla \cdot (\alpha_\varphi \rho_\varphi \boldsymbol{U}_\varphi \boldsymbol{U}_\varphi) - \nabla \cdot (\alpha_\varphi \rho_\varphi \tau_\varphi) = -\alpha_\varphi \nabla p + \alpha_\varphi \rho_\varphi \boldsymbol{g} + \sum \boldsymbol{F}_i, \tag{2}$$

where the subscript φ in the formulas is used to distinguish a specific phase, representing the physical quantities of water and air, respectively. In this study, the subscript w denotes the water phase, and the subscript a denotes the air phase. α represents the phase fraction, ρ denotes the density, $\boldsymbol{U}$ stands for velocity, p is the pressure, $\boldsymbol{g}$ is the gravitational acceleration, and $\boldsymbol{F}_i$ denotes the interphase forces.

In the Euler–Euler method, the interphase force $\boldsymbol{F}_i$ is a very important source term, representing the mutual interaction force between the two fluids. Typically, $\boldsymbol{F}_i$ includes drag force $\boldsymbol{F}_\mathrm{d}$, lift force $\boldsymbol{F}_\mathrm{l}$, turbulent diffusion force $\boldsymbol{F}_\mathrm{t}$, virtual mass force $\boldsymbol{F}_\mathrm{v}$, wall lubrication force $\boldsymbol{F}_\mathrm{w}$, etc. Among them, the most important is the drag force $\boldsymbol{F}_\mathrm{d}$ of one phase on the other, which can be expressed as

$$\boldsymbol{F}_\mathrm{d} = \frac{3}{4}\rho_\mathrm{w}\alpha_\mathrm{a}C_\mathrm{d}\frac{1}{d_\mathrm{a}}|\boldsymbol{U}_\mathrm{w} - \boldsymbol{U}_\mathrm{a}|(\boldsymbol{U}_\mathrm{w} - \boldsymbol{U}_\mathrm{a}), \tag{3}$$

where ρ_w and α_a represent the density of water and the volume fraction of air, respectively. C_d denotes the drag coefficient of the bubbles, d_a is the bubble diameter, and $\boldsymbol{U}_\mathrm{w}$ and $\boldsymbol{U}_\mathrm{a}$ represent the velocities of water and air, respectively. Here, $\boldsymbol{F}_\mathrm{d}$ denotes the drag force acting on the dispersed phase (air) from the continuous phase (water). The sign convention follows the velocity difference term ($\boldsymbol{U}_\mathrm{w} - \boldsymbol{U}_\mathrm{a}$): a positive value indicates that the air phase is accelerated by the water phase. The drag force acting on the water phase is $\boldsymbol{F}_\mathrm{d,w} = -\boldsymbol{F}_\mathrm{d,a}$. In this study, the drag coefficient term C_d is calculated using the Schiller–Naumann model,[20] which is expressed as follows:

$$C_\mathrm{d} = \begin{cases} \frac{24}{\mathrm{Re}}(1 + 0.15Re^{0.687}), & \mathrm{Re} < 1000, \\ 0.44, & \mathrm{Re} \geq 1000, \end{cases} \tag{4}$$

where Re represents the Reynolds number of the spherical particle, calculated based on the particle's diameter.

As for the lift force $\boldsymbol{F}_\mathrm{l}$ on the dispersed phase, relevant derivations and calculation methods have been proposed by Drew and Lahey.[30] In OpenFOAM, the lift force $\boldsymbol{F}_\mathrm{l}$ is expressed as

$$\boldsymbol{F}_\mathrm{l} = C_\mathrm{L} \cdot \rho_\mathrm{w} \cdot (\boldsymbol{U}_\mathrm{r} \times (\nabla \times \boldsymbol{U}_\mathrm{w})), \tag{5}$$

where ρ_w represents the density of the continuous phase (water), $\boldsymbol{U}_\mathrm{r} = \boldsymbol{U}_\mathrm{a} - \boldsymbol{U}_\mathrm{w}$ is the relative velocity, $\nabla \times \boldsymbol{U}_\mathrm{w}$ is the vorticity of the continuous phase, and C_L is the lift coefficient, which is calculated using the lift model proposed by Tomiyama *et al.*[22] Its expression is as follows:

$$C_\mathrm{L} = \begin{cases} \min\left(0.288\tanh(0.121Re), f(E_\mathrm{OH})\right), & E_\mathrm{OH} < 4, \\ f(E_\mathrm{OH}), & 4 \leq E_\mathrm{OH} \leq 10.7, \\ -0.288, & E_\mathrm{OH} > 10.7, \end{cases} \tag{6}$$

where Re is the relative Reynolds number of the bubble, and E_OH is the modified Eötvös number, which is based on the maximum horizontal dimension of the deformed bubble. It is typically calculated by $E_\mathrm{OH} = \boldsymbol{g}\Delta\rho D_\mathrm{H}^2/\sigma$. Here, $\boldsymbol{g}$ is the gravitational acceleration, taken as 9.8 m/s^2; $\Delta\rho$ is the density difference between the two phases; D_H is the bubble diameter; and σ is the surface tension coefficient, approximately 0.072 N/m. The function $f(E_\mathrm{OH})$ is calculated as follows:

$$f(E_\mathrm{OH}) = 0.0010423E_\mathrm{OH}^3 - 0.0159E_\mathrm{OH}^2 - 0.0204E_\mathrm{OH} + 0.474. \tag{7}$$

The turbulent dispersion force $\boldsymbol{F}_\mathrm{t}$ is used to move the dispersed phase toward regions of lower turbulence intensity. It manifests as a diffusion-like phenomenon, making the distribution of the dispersed phase more uniform and preventing local accumulation. The turbulence dispersion force model can be expressed as follows:[31]

$$\boldsymbol{F}_\mathrm{t} = 0.75 \cdot (C_\mathrm{D}Re) \cdot \frac{\nu_\mathrm{w}\nu_\mathrm{t}}{\sigma \cdot d_\mathrm{d}^2} \cdot \rho_\mathrm{w}\alpha_\mathrm{a} \cdot \left(\frac{1}{\max(\alpha_\mathrm{a}, \alpha_\mathrm{res})} + \frac{1}{\max(\alpha_\mathrm{w}, \alpha_\mathrm{res})}\right), \tag{8}$$

where C_D is the drag coefficient, Re is the Reynolds number, ν_w and ν_t are the molecular kinematic viscosity and turbulent kinematic viscosity of the continuous phase, respectively, ρ_w is the density of the continuous phase, α_a is the volume fraction of the dispersed phase, α_res is the residual volume fraction, α_w is the volume fraction of the continuous phase, and σ is the turbulent Schmidt number, which is typically 0.7.

The virtual mass force $\boldsymbol{F}_\mathrm{v}$ stems from the additional inertial effect when an accelerating bubble induces the surrounding fluid to accelerate simultaneously. It can be expressed as

$$\boldsymbol{F}_\mathrm{v} = \alpha_\mathrm{a}\rho_\mathrm{w}C_\mathrm{vm}\left[\frac{D\boldsymbol{U}_\mathrm{w}}{Dt} - \frac{D\boldsymbol{U}_\mathrm{a}}{Dt}\right], \tag{9}$$

where the coefficient C_vm is from the analytical solution in potential flow theory for the accelerated motion of a spherical object in an unbounded, inviscid fluid. For a sphere, the added mass equals half the mass of the displaced fluid, yielding a coefficient of $C_\mathrm{vm} = 0.5$. The $D/Dt = \partial/\partial t + \boldsymbol{U} \cdot \nabla$ denotes the material derivative, representing the acceleration following the motion of each phase.

The wall lubrication force $\boldsymbol{F}_\mathrm{w}$ is used to simulate the normal force experienced by the dispersed phase (bubbles) when approaching the wall, which pushes the dispersed phase away from the wall. It can be expressed as[32]

$$\boldsymbol{F}_\mathrm{w} = \max\left(0, \frac{C_\mathrm{w1}}{d_\mathrm{d}} + \frac{C_\mathrm{w2}}{y}\right)\rho_\mathrm{w}|\boldsymbol{U}_{\mathrm{r},\parallel}|^2\boldsymbol{n}, \tag{10}$$

where d_d represents the bubble diameter; C_w1 denotes the first wall lubrication coefficient, typically taken as -0.01; C_w2 denotes the second wall lubrication coefficient, typically taken as 0.05; y is the distance to the wall; ρ_w is the density of the continuous phase; $\boldsymbol{U}_\mathrm{r}$ is the tangential component of the relative velocity with respect to the wall; $|\boldsymbol{U}_{\mathrm{r},\parallel}|^2 = |\boldsymbol{U}_\mathrm{r} - (\boldsymbol{U}_\mathrm{r} \cdot \boldsymbol{n})\boldsymbol{n}|^2$; and $\boldsymbol{n}$ is the unit normal vector to the wall.

τ_φ represents the effective stress. In this study, the subgrid-scale (SGS) stress is solved using the Smagorinsky model.[33] The Smagorinsky model is a subgrid-scale (SGS) model used in large eddy simulation (LES), which accounts for the effects of small-scale turbulence on the large-scale flow by introducing a turbulent viscosity (eddy viscosity). This model is based on the equilibrium assumption, i.e., that the production and dissipation of kinetic energy at the

22 October 2026 13:43:54

Published under an exclusive license by AIP Publishing

subgrid scale are in local equilibrium. The Smagorinsky model adopts the Boussinesq hypothesis, which relates the subgrid-scale stress to the strain rate tensor of the resolved scales as follows:

$$\tau_{ij}^{\mathrm{sgs}} = \frac{2}{3}k_{\mathrm{sgs}}\delta_{ij} - 2\nu_{\mathrm{sgs}}\bar{S}_{ij}, \tag{11}$$

where k_{sgs} is the subgrid-scale turbulent kinetic energy, ν_{sgs} is the subgrid-scale eddy viscosity coefficient, and S_{ij} is the resolved-scale strain rate tensor, which can be expressed as

$$S_{ij} = \frac{1}{2}\left(\frac{\partial \bar{u}_i}{\partial x_j} + \frac{\partial \bar{u}_j}{\partial x_i}\right). \tag{12}$$

ν_{sgs} is the subgrid-scale eddy viscosity coefficient, which is calculated in the Smagorinsky model by the following equation:

$$\nu_{\mathrm{sgs}} = (C_s\Delta)^2|\bar{S}|, \tag{13}$$

where C_s is the Smagorinsky constant, which depends on the flow conditions and is typically taken as 0.17. Δ is the filter scale, defined as the cube root of the grid volume, and $|S|$ is the magnitude of the strain rate tensor, which can be expressed by the following equation:

$$|\bar{S}| = \sqrt{2\bar{S}_{ij}\bar{S}_{ij}}. \tag{14}$$

In the present simulations, the algebraic Smagorinsky relation [Eq. (13)] is used directly to compute the subgrid-scale eddy viscosity, which is the standard implementation of the Smagorinsky model in OpenFOAM. The isotropic term $\frac{2}{3}k_{sgs}\delta_{ij}$ in the SGS stress tensor is absorbed into the modified pressure $\tilde{p} = p + \frac{2}{3}\rho k_{sgs}$, which is a standard practice in LES implementations. Therefore, only the deviatoric part of the SGS stress appears through the effective viscosity in Eq. (15).

Finally, the turbulent viscosity ν_{sgs} is obtained. Subsequently, the turbulent viscosity is added to the molecular viscosity to obtain the effective viscosity $\nu_{\mathrm{eff}} = \nu + \nu_{\mathrm{sgs}}$, which is then substituted into the following equation to calculate the shear stress:

$$\boldsymbol{\tau}_\phi = -\boldsymbol{\nu}_{\varphi,\mathrm{eff}}\left[\nabla \boldsymbol{U}_\phi + \nabla^{\mathrm{T}}\boldsymbol{U}_\phi\right] + \frac{2}{3}\boldsymbol{\nu}_{\varphi,\mathrm{eff}}\nabla\cdot(\boldsymbol{U}_\phi\cdot\boldsymbol{I}). \tag{15}$$

It should be noted that the interphase-force closures employed in this study (drag, lift, virtual mass, and wall lubrication) are originally developed for dilute bubbly flows with spherical or mildly deformed bubbles. In high-void-fraction regions, such as the continuous air layer beneath the hull ($\alpha_a \gtrsim 0.1$), these closures may not accurately represent the momentum exchange between phases. However, in these regions the flow is dominated by buoyancy, gravity, and geometric constraints, and the influence of interphase force models on the overall air-layer morphology is considered secondary. In the stern wake region, where most of the present analyses are focused, the local void fraction is significantly lower and the dispersed-phase assumptions are more appropriate. The $\alpha_a = 0.5$ isosurface is used solely as a visualization tool and does not imply interface resolution in the sense of VOF or level-set methods.

B. IATE approach

Since there are a large number of discrete bubbles in ship ALDR, and the bubbles continuously coalesce and break up during the flow, it is very important to consider how the changes in bubbles affect the flow. To further calculate the motion and distribution of bubbles in the flow, the interfacial area transport equation (IATE) is used.[34] The IATE is implemented by solving an additional transport equation for the interfacial area density, which accounts for bubble coalescence and breakup through source and sink terms. These terms are modeled using semi-empirical closures that depend on local flow conditions such as turbulence, surface tension, and viscosity. The predicted interfacial area is then coupled with the Eulerian two-fluid solver to influence interphase momentum transfer, enabling the simulation of bubble dynamics without explicitly resolving individual bubble interfaces. Its expression is as follows:

$$\frac{\partial a_i}{\partial t} + \nabla\cdot(a_i\boldsymbol{U}_i) = \frac{2}{3}\left(\frac{a_i}{\alpha}\right)\left(\frac{\partial \alpha}{\partial t} + \nabla\cdot\alpha\boldsymbol{U}_{\mathrm{a}} - \eta_{\mathrm{ph}}\right) + \frac{1}{3\psi}\left(\frac{\alpha}{a_i}\right)^2\sum_j \boldsymbol{R}_j + \pi D_{\mathrm{bc}}^2 R_{\mathrm{ph}}, \tag{16}$$

where a_i denotes the interfacial area concentration, which is calculated as $n \times A_i$, where n represents the number of particles per unit volume and A_i denotes the average surface area of a particle. $\boldsymbol{U}_i$ is the interfacial velocity, α stands for the phase fraction, and $\boldsymbol{U}_{\mathrm{a}}$ represents the air-phase velocity. η_{ph} denotes the rate of volume generated by nucleation per unit mixture volume. In the one-group interfacial area transport equation, ψ can be calculated as $1/36\pi$. $\boldsymbol{R}_j$ denotes the net source term for the interfacial area concentration, representing the combined effect of bubble coalescence and breakup. Physically, it accounts for the rate at which the interfacial area per unit mixture volume changes due to these two competing mechanisms: coalescence reduces the total interfacial area by merging smaller bubbles into larger ones, acting as a sink term; breakup increases the interfacial area by splitting larger bubbles into smaller ones, acting as a source term. The term is modeled through semi-empirical closures that consider local flow conditions, such as turbulence intensity, surface tension, and bubble collision frequencies. The unit of $\boldsymbol{R}_j$ is reciprocal meters per second, consistent with the transport equation for interfacial area concentration. D_{bc} is the critical bubble size, and R_{ph} represents changes due to phase transition, which are not considered in this context.

In the IATE model, $\boldsymbol{R}_j$ represents bubble–fluid interaction mechanisms and primarily encompasses three forms: (1) disintegration due to the impact of turbulent eddies; (2) coalescence through random collisions; and (3) coalescence due to the acceleration of a trailing bubble within the wake of a preceding bubble.[35] The expression is given as

$$R_{\mathrm{TI}} = C_{\mathrm{TI}}\left(\frac{nu_t}{D_{\mathrm{b}}}\right)\exp\left(-\frac{We_{\mathrm{cr}}}{We}\right)\sqrt{1-\frac{We_{\mathrm{cr}}}{We}}, \tag{17}$$

$$R_{\mathrm{RC}} = C_{\mathrm{RC}}\left[\frac{n^2 u_t D_{\mathrm{b}}^2}{\alpha_{\max}^{1/3}(\alpha_{\max}^{1/3}-\alpha^{1/3})}\right]\times\left[1-\exp\left(-C\frac{\alpha_{\max}^{1/3}\alpha^{1/3}}{\alpha_{\max}^{1/3}-\alpha^{1/3}}\right)\right], \tag{18}$$

$$R_{\mathrm{WE}} = C_{\mathrm{WE}}C_{\mathrm{D}}^{1/3}(D_{\mathrm{b}})n^2 D_{\mathrm{b}}^2 u_{\mathrm{r}}(D_{\mathrm{b}}), \tag{19}$$

where the first equation is valid only when $We > We_{cr}$, and the C_{TI} is a coefficient determined experimentally, n is the number density of bubbles, and u_t is turbulent fluctuating velocity. In the present OpenFOAM implementation, the turbulent fluctuating velocity u_t appearing in the breakup source term [Eq. (17)] is computed from

22 October 2026 13:43:54

Published under an exclusive license by AIP Publishing

the turbulent kinetic energy of the continuous phase via $u_t = \sqrt{2k_w}$, where k_w is the turbulent kinetic energy of the water phase (in the present LES framework, corresponding to the subgrid-scale turbulent kinetic energy k_{sgs}). D_b is the bubble diameter, and We_{cr} is the critical Weber number. In the second equation, C_{RC} and C are coalescence coefficients derived from experiments, and α_{max} denotes the maximum packing limit. In the third equation, C_{WE} represents the coalescence coefficient determined experimentally, and C_D denotes the drag coefficient. In this study, the values for the respective coefficients are set based on the results provided by Ishii as follows: $C_{TI} = 0.085$, $We_{cr} = 6.0$, $C_{RC} = 0.004$, $C = 3.0$, $\alpha_{max} = 0.75$, and $C_{WE} = 0.002$.

C. Numerical setup

The numerical simulations in this study are conducted using the open-source CFD software OpenFOAM. The ship model investigated in this study is a specially designed KVLCC equipped with an ALDR system on its bottom, as shown in Fig. 1(a). The model has a length between perpendiculars (L_{pp}) of 7 m, corresponding to a scale ratio of 1:42, and a design speed of 15 knots. At model scale, the experimental speed is 1.117 m/s.

The air-layer device on the ship's bottom consists of two main components. The first is a longitudinal air barrier along the hull, whose primary function is to prevent air dispersion from the sides and maintain a stable air-layer structure. The second component comprises wedge-shaped structures at the bow and stern. The bow wedge is designed to induce flow separation, facilitating air accumulation and layer formation after injection from the holes. The stern wedge serves to promote air-layer accumulation and stabilize the mixed flow exiting the bottom air-layer region, as illustrated in Fig. 1(b). The heights of the bow wedge, stern wedge, and air barrier h are all 1 cm. Three rows of air injection holes, designated A1–A3 from bow to stern, are arranged on the bottom of ship, as shown in Fig. 2. Their longitudinal positions are $x_{A1}/L_{pp} = 0.1743$, $x_{A2}/L_{pp} = 0.2955$, and $x_{A3}/L_{pp} = 0.5642$, respectively. The number of holes in each row is as follows: nA1 = 8, nA2 = 10, and nA3 = 10. In the physical model tests, the holes are circular. However, due to meshing difficulties associated with circular holes in numerical simulations, square holes are employed instead. The injection velocities for the numerical simulations are derived by equating the flow area and volumetric flow rate, resulting in $V_{A1} = 1.915$ m/s, $V_{A2} = 0.5347$ m/s, and $V_{A3} = 0.8377$ m/s.

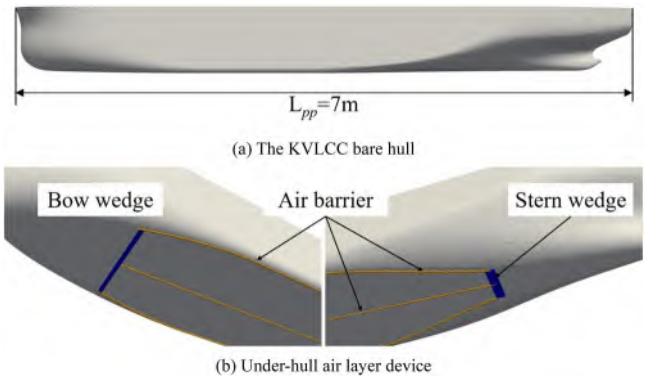

FIG. 1. Schematic of the KVLCC ship model (a) and ALDR devices (b).

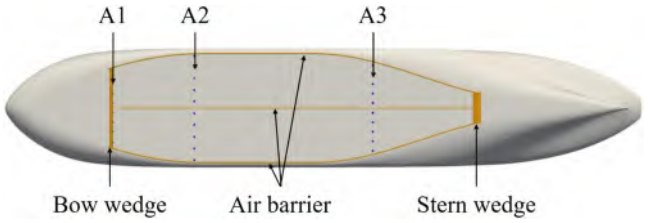

FIG. 2. Schematic of the bottom air-layer device and air injection holes.

The bubble diameter is set within the range of $D_b = 0.5$–1.0 mm, consistent with experimental observations for microbubble generation through submerged orifices under similar flow conditions. In the present IATE-based formulation, the local bubble diameter is not prescribed as a single constant value, but is obtained from the interfacial curvature field as $D_b = 6/\kappa$, with the maximum and minimum diameter limits set to $D_{b,max} = 1.0$ mm and $D_{b,min} = 0.5$ mm. The corresponding injection Reynolds and Weber numbers (based on $D_b = 0.75$ mm) are $Re_{A1} \approx 97$, $Re_{A2} \approx 27$, and $Re_{A3} \approx 43$ and $We_{A1} \approx 38.2$, $We_{A2} \approx 3$, and $We_{A3} \approx 7.3$, which fall within the bubbly flow regime.

The principal parameters of the ship model and the ALDR devices are summarized in Table I.

This study focuses on the numerical simulation of ALDR effects without considering free-surface influence. Therefore, a double-model approach is adopted, where the computational top boundary of domain coincides with the undisturbed waterline, considering only the submerged part of the hull. The gravity direction is aligned with the z axis, and the flow direction corresponds to the x axis. The top boundary of the domain is aligned with the waterline and treated as a symmetry plane. It should be emphasized that a symmetry plane enforces zero normal flux, so air cannot escape through the top boundary and buoyant air tends to accumulate beneath it. This differs from a physical free surface, where part of the air would escape to the atmosphere. This treatment is consistent with the double-model idealization adopted in this study. While this differs from a physical free surface where air would partially escape, the top boundary is located

TABLE I. Characteristics of the KVLCC model and ALDR devices.

Length between perpendiculars	L_{pp} (m)	7
Length of waterline	L_{WL} (m)	6.9688
Draft	T (m)	0.4295
Beam of waterline	B_{WL} (m)	1.257
Depth	D (m)	0.721
Block coefficient	$\nabla/(L_{pp}\, B_{WL} T)$	0.778
Displacement volume	∇ (m^3)	2.9387
Height of air-layer devices	h (cm)	1
Location of A1	x_{A1}/L_{pp}	0.1743
Location of A2	x_{A2}/L_{pp}	0.2955
Location of A3	x_{A3}/L_{pp}	0.5642
Air velocity of A1 (V_{A1})	m/s	1.915
Air velocity of A2 (V_{A2})	m/s	0.5347
Air velocity of A3 (V_{A3})	m/s	0.8377

22 October 2026 13:43:54

Published under an exclusive license by AIP Publishing

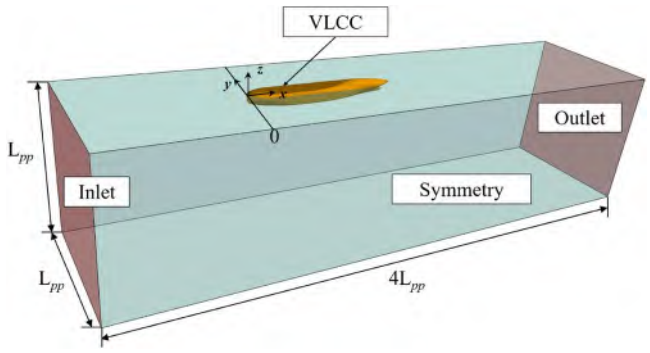

FIG. 3. Schematic of computational domain.

at a considerable distance above the propeller disk, and the buoyancy-driven upward velocity is much smaller than the streamwise advection. The influence of this boundary treatment on the flow field and air distribution at the propeller disk plane is therefore considered to be limited. The left, right, and bottom boundaries of the computational domain are symmetric boundaries, the inlet boundary is a uniform velocity inlet boundary, and the outlet is a zero-gradient non-reflective outlet. The domain extends $4L_{pp}$ in the streamwise direction, $1L_{pp}$ in depth, and $1L_{pp}$ in width. The bow is located at $x = 0$, positioned $1L_{pp}$ downstream from the domain inlet, as shown in Fig. 3.

The computational mesh is generated using the snappyHexMesh utility in OpenFOAM. Given the relatively small size of the bottom air-layer devices compared to the hull, these regions are meshed separately with higher levels of refinement, as depicted in Fig. 4. To satisfy the requirements for simulating air–water mixed flows while maintaining numerical efficiency for engineering applications, the present LES is performed within the framework of LES with wall functions (also referred to as wall-modeled LES, WMLES), rather than wall-resolved LES. This choice is made considering the practical constraints of simulating a model-scale ship hull with complex bottom air-layer devices, where a fully wall-resolved LES would be computationally prohibitive. In the present simulations, the Smagorinsky subgrid-scale model is employed, and the near-wall turbulent viscosity is treated via the "nutkWallFunction" boundary condition in OpenFOAM, which computes ν_t at the first grid node using the standard wall-function approach. Accordingly, a y^+ value in the range of 30–100 is considered adequate for the wall-function-based LES framework. The final mesh yields an average y^+ of 60, with even lower y^+ values achieved in the vicinity of the under-hull air-layer device, and the streamwise and spanwise resolutions are $\Delta x^+ \approx 146$ and $\Delta z^+ \approx 122$, respectively, which are sufficient to resolve the outer-layer large-scale turbulent structures, while the near-wall viscous sublayer is modeled via the wall function. Furthermore, local grid refinement is applied to the wake region.

The physical time step is $\Delta t = 1.0 \times 10^{-4}$ s. A single-phase flow calculation was first performed for 30 s to establish a fully developed inflow condition, after which air injection was activated and the two-phase flow calculation was continued for an additional 30 s. To exclude the initial transient period following the activation of air injection, time averaging was initiated after 15 s of two-phase flow simulation, by which time the flow had reached a statistically stationary state, as judged by monitoring the time history of the air volume fraction beneath the hull and the total resistance coefficient. The averaging window therefore covers a physical duration of 15 s, corresponding to approximately 2.4 flow-through times ($L_{pp}/U_0 \approx 7/1.117 \approx 6.27$ s). During the averaging window, solution fields were sampled every time step ($\Delta t = 1.0 \times 10^{-4}$ s) for time averaging. While the monitored quantities exhibited only minor fluctuations during the averaging window, a formal statistical convergence analysis was not performed; the time-averaged results presented in this study should therefore be interpreted as representative mean values over the sampled period.

D. Numerical verification and validation

Since the physical model experiments for ship air-layer drag reduction mainly focus on the measurement of the ship stern wake, including both air-entrained and single-phase conditions, while the distribution and evolution of the air layer beneath the hull are not quantitatively analyzed, the grid independence verification and numerical validation in this study are carried out from two aspects. The first is the comparison of the mean wake fraction at the propeller disk plane under single-phase flow (single-phase) conditions. The second is the comparison of the mean wake fraction at the propeller disk plane under air-entrained conditions with air-layer drag reduction. In both experimental conditions, the ship model (with an air-layer device installed at the bottom) and the inflow velocity are identical. A total of three sets of grids with different cell counts were designed for the numerical simulation: 8.84×10^6 (coarse mesh), 12.5×10^6 (medium mesh), and 17.7×10^6 (fine mesh). In the experiments, the mean wake fraction was measured at nine different radial positions on the propeller disk plane ($r/R = 0.4$–1.2, where r is the measured radius and R is the propeller radius), and the overall mean wake fraction w_{mean} was finally calculated using the following formula:

$$w_{\text{mean}} = \frac{\sum (w_r \cdot (r/R))}{\sum (r/R)}, \tag{20}$$

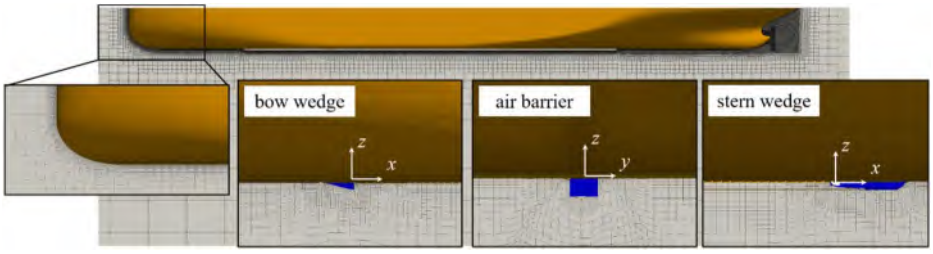

FIG. 4. Schematic of computational mesh around the hull and the air-layer device.

22 October 2026 13:43:54

Published under an exclusive license by AIP Publishing

TABLE II. Grid sensitivity study of calculated mean wake fraction at the propeller disk plane. (Positive errors indicate CFD overestimation relative to experiments; negative errors indicate underestimation.)

Mesh	EXP-single-phase	CFD-single-phase	Error (%)	EXP-air-entrained	CFD-air-entrained	Error (%)
Coarse	0.2956	0.3196	8.12	0.1750	0.1530	−12.57
Medium		0.3159	6.89		0.1582	−9.60
Fine		0.3152	6.63		0.1604	−8.34

where w_r represents the mean wake fraction at a given radius, and r/R denotes the ratio of the actual radius to the propeller radius. The final computational results are shown in Table II.

It can be seen from the results that the calculated mean wake fraction with the medium mesh is not significantly different from that with the fine mesh, while both differ considerably from the coarse mesh results. Under single-phase conditions, the overall calculated mean wake fraction is slightly higher than the experimental value. The difference in the percentage error relative to the experiment between the medium and fine meshes is 0.26%, and that between the medium and coarse meshes is 1.23%. Under air-entrained conditions, the difference in the percentage error relative to the experiment between the medium and fine meshes is 1.26%, and that between the medium and coarse meshes is 2.97%. This indicates that using the medium mesh yields sufficiently accurate results, and further increasing the grid resolution offers little improvement in computational accuracy. Therefore, the medium mesh will be used for subsequent calculations. Figure 5 below shows the contour of the mean wake fraction at the propeller disk plane obtained using the medium mesh. Figure 6 shows the calculated mean wake fraction at each radius under single-phase and air-entrained conditions.

The computational results indicate that the Euler–Euler method combined with the IATE approach reproduces the mean wake fraction at the propeller disk plane with errors of 6.89% and −9.6% under single-phase and air-entrained conditions, respectively, using the medium mesh. Considering the computational mesh, the choice of turbulence model, and the inherent complexity of air–water mixed flows, the numerical methods and meshing strategy adopted in this study are considered adequate for subsequent investigations into the mixed-flow characteristics of ALDR ships and the air-entrained wake flow at the stern.

It should be noted that the present validation is primarily based on the mean wake fraction at the propeller disk plane, which is the only quantitative experimental data available for the present ship model under both single-phase and air-entrained conditions. Systematic grid sensitivity analyses for other key quantities, such as air-layer thickness, air fraction distribution, and vortex structures, have not been performed due to the substantial computational cost. Therefore, the mechanistic interpretations presented in Secs. III A–III C are offered as qualitative observations based on the present simulation setup, and further validation with additional experimental data and systematic grid refinement is needed to fully confirm these findings.

III. RESULTS AND DISCUSSION

A. Air-layer characteristics of hull bottom

The time-averaged quantities presented in this section were obtained over an averaging window of 15 s, following an initial transient period of 15 s after the activation of air injection. During this

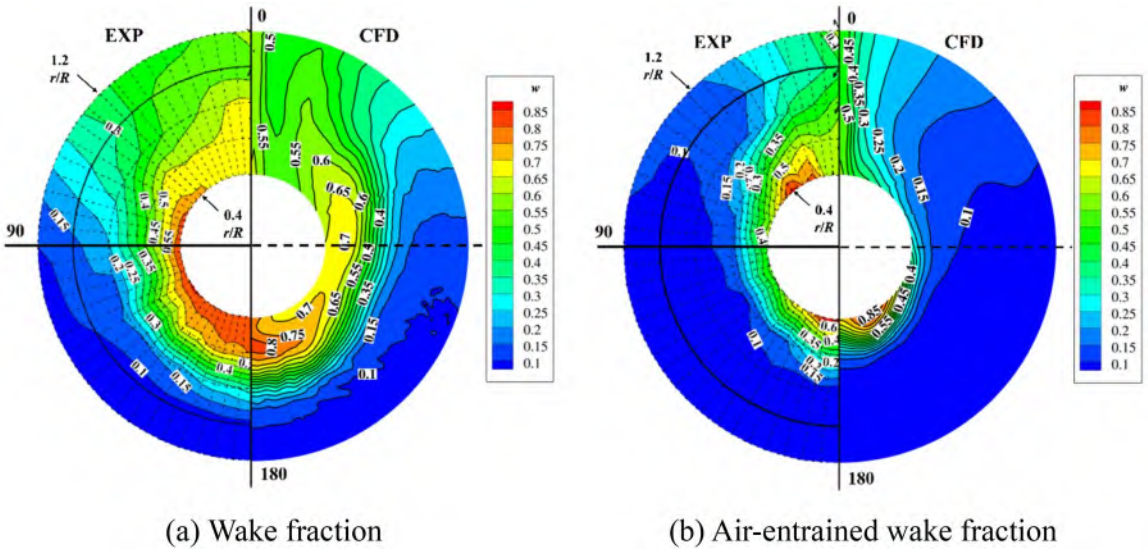

FIG. 5. Comparison between numerical calculation results and experimental results of the mean wake fraction at the propeller disk plane ($x/L_{pp} = 0.9586$).

22 October 2026 13:43:54

Published under an exclusive license by AIP Publishing

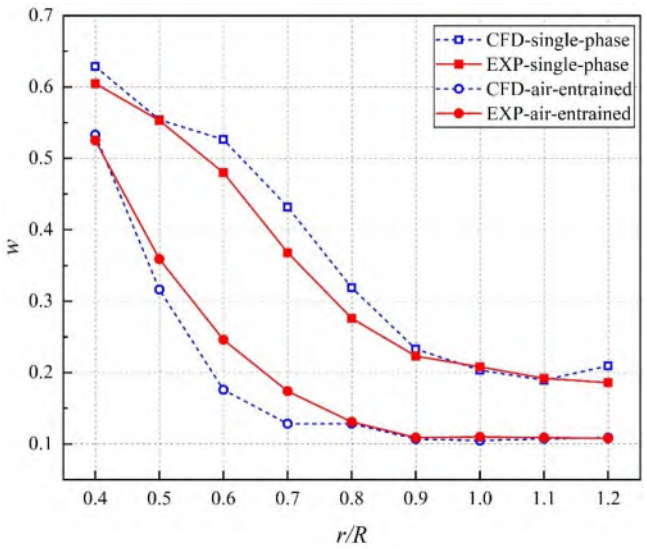

FIG. 6. Comparison of mean wake fraction at each radius of the propeller disk plane (x/L_pp = 0.9586) between numerical calculations and experiments.

window, the monitored air volume fraction beneath the hull varied within a narrow band, indicating that a statistically stationary state had been approximately achieved. The instantaneous snapshots are representative of the unsteady flow behavior within this window.

After the flow becomes fully developed, Fig. 7(a) presents the top-view contour plots of the air volume fraction at the ship bottom and stern. Under the effect of the bow wedge, the air layer beneath the hull is unable to spread upstream of the wedge, and a distinct air–water interface is formed immediately behind the wedge. Meanwhile, the step effect induced by the flow passing over the wedge generates a recirculation zone. This prevents the air injected from the first row of air holes from being rapidly swept away by the flow downstream of the wedge, while simultaneously increasing the local turbulence intensity, which renders the air unable to remain stable, manifesting as a reduction in the local air volume fraction. However, owing to buoyancy and accumulation, the air subsequently re-aggregates to form an air layer at the bottom. Downstream of the second row of air holes, the increased air injection rate leads to a rise in the total air content beneath the hull. At this stage, the mixed flow is no longer affected by the bow wedge and tends toward a relatively steady state, allowing the air to continuously accumulate and form a continuous air layer along the mid-bottom region. As the water–air interface becomes unstable, the continuous air layer loses its stability and transitions into a dispersed air–water flow, accompanied by a decrease in air content near the bottom wall. Further downstream, at the third row of air holes, the air supply is replenished, reestablishing a continuous air layer that covers a substantial area of the aft bottom region.

Figure 7(b) shows the morphology of the air layer at the bottom of the ship in the model experiment. The numerical results reproduce the main morphological features of the experimental air layer, including the overall streamwise extent and the accumulation–instability–reaccumulation pattern, although local differences remain in the region immediately behind the first row of air holes, where the air layer is more stable in the experiment than in the simulation. A

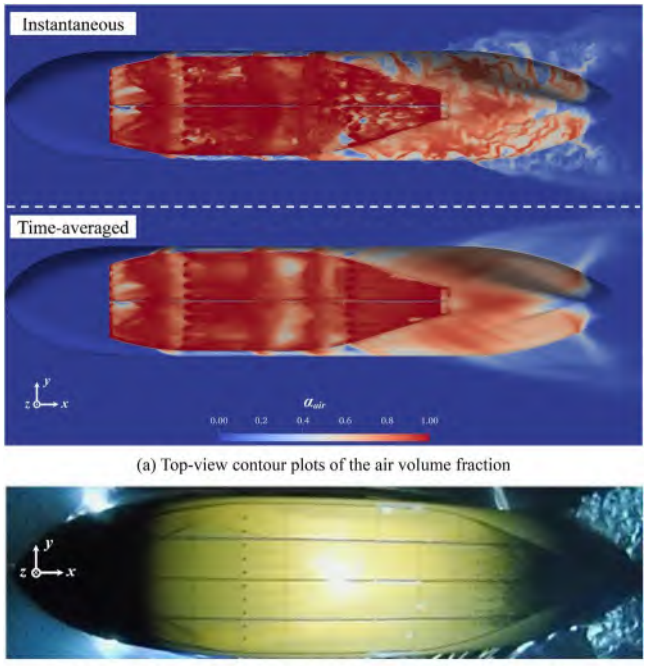

(a) Top-view contour plots of the air volume fraction

(b) Morphology and distribution of the air layer at the bottom (bottom view)

FIG. 7. Instantaneous and time-averaged top-view contour plots of the air volume fraction at the ship bottom and stern.

possible reason is that the wedge-shaped bow structure is relatively small, resulting in insufficient mesh resolution for capturing the geometry. In addition, the local calculation accuracy may be reduced due to abrupt transitions in mesh density.

Figure 8 shows the distribution of the air layer beneath the ship hull. Since the Euler–Euler method does not explicitly capture the air–water interface, the interface is identified using the commonly adopted criterion from the VOF method, i.e., the isosurface at a phase fraction of 0.5 is taken as the water–air interface, colored by the air-phase velocity. It can be observed from the figure that the bottom of the ship is largely covered by air, maintaining a continuous air layer. The flow velocity at the interface is relatively low, indicating a distinct velocity difference across the air–water interface; such a velocity difference is expected to contribute to a reduction in frictional resistance, although the wall shear stress is not quantified in the present study. Under the influence of the air dams on both sides, the air is prevented from spreading laterally in the forward and middle sections of the ship bottom, and gradually flows toward the stern, forming an air layer. At the stern, the accumulation of air causes the air-layer thickness to exceed the height of the air dams, leading to air spillage and rapid upward rise along the side walls of the stern. This phenomenon is also corroborated by the air-phase velocity at the stern, where the velocity on both sides of the stern exhibits a significant increase due to the superposition of the upward velocity and the streamwise velocity.

Figure 9 presents the distribution of air-layer thickness between the region immediately downstream of the first row of injection holes (A1) and the second row (A2), with the air volume fraction of 0.5 defined as the air–water interface. Given that the flow field is essentially symmetric in the horizontal direction, only one side (from the

22 October 2026 13:43:54

Published under an exclusive license by AIP Publishing

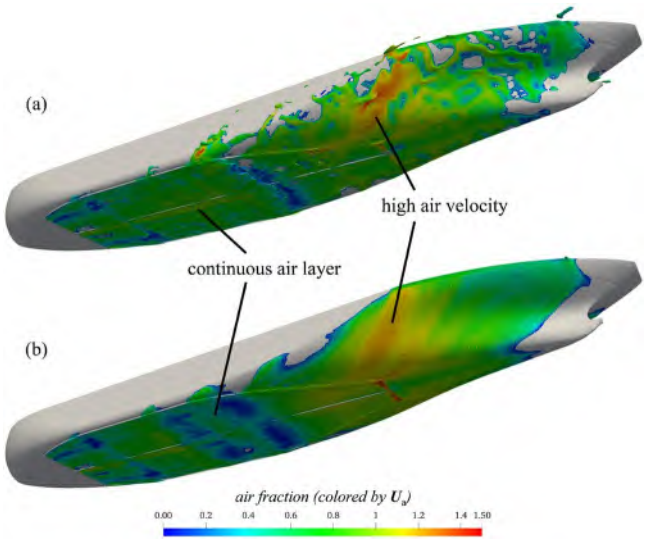

FIG. 8. Contour plots of the air-layer distribution under the ship bottom at instantaneous (a) and time-averaged (b) states (isosurface at an air fraction of 0.5, colored by air velocity).

centerline to the positive y direction) is selected for analysis. Here, x_{A1} denotes the streamwise position of the first row of injection holes, x_{A2} denotes the streamwise position of the second row, and x represents the streamwise coordinate at a given location. Accordingly, the abscissa in the figure represents the ratio of the downstream distance from the first row of air holes to the streamwise spacing between the two rows. The ordinate denotes the dimensionless air-layer thickness t_{air}/h, which is calculated by the ratio of the actual thickness of the air layer t_{air} (cm), to the height of the air-layer devices, h (cm). The upper panel shows the instantaneous results, while the lower panel presents the time-averaged results.

It can be observed from the figure that the overall air-layer thickness exhibits a trend of initially increasing and then decreasing sharply. Immediately after the air is injected from the holes, the vertical momentum component normal to the flow direction leads to a locally increased air-layer thickness; however, this thickness is rapidly reduced as the air is swept downstream by the water flow. As the air gradually accumulates, the air-layer thickness increases, reaching a maximum time-averaged value of approximately 1.3–1.6 cm. When the air layer attains its maximum height, the interfacial instability is triggered, and the air–water interface exhibits a flow regime similar to wave breaking, resulting in a sharp reduction in air-layer thickness. This behavior can be interpreted within the framework of classical interfacial instability theory. The velocity shear between the air layer and the surrounding water flow gives rise to Kelvin–Helmholtz (KH)-type instability, under which interfacial waves grow and eventually reach a critical amplitude.[36,37] The subsequent sharp reduction in air-layer thickness is analogous to the spilling breaker phenomenon in free-surface flows.[38,39]

Among the possible contributing factors, the velocity shear between the air layer and the surrounding water is considered the primary driver of the KH-type instability. In addition, the adverse pressure gradient along the hull bottom, particularly in the stern region,

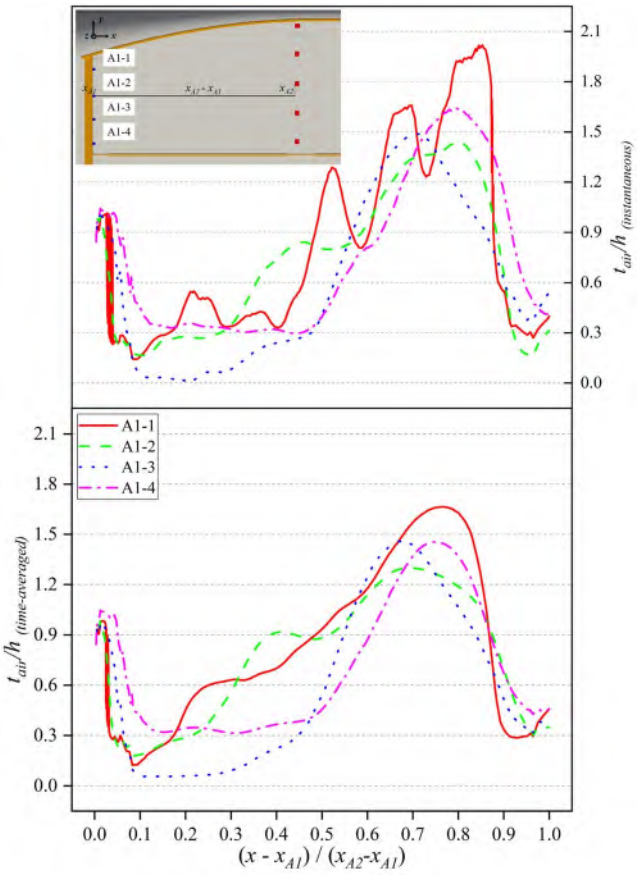

FIG. 9. Distribution of air-layer thickness t_{air} (air fraction = 0.5) between the first row of air holes (A1) and the second row (A2), instantaneous (upper), and time-averaged (lower).

further destabilizes the interface by reducing the effective stability margin.[40] The recirculation zone downstream of the bow wedge introduces local velocity fluctuations that act as a triggering perturbation for the instability. Thus, KH instability is considered the primary mechanism, while the wedge-induced recirculation serves as an amplifying trigger and the pressure gradient provides a background destabilizing condition.

The presence of turbulent vortices near the interface further promotes local velocity fluctuations and accelerates the breakup process. These mechanisms are consistent with recent findings in air lubrication flows, where interface instability is closely linked to unsteady vortex dynamics in the near-wall region. In the spanwise direction, the air-layer thickness is smaller in the central region and larger near the two sides, indicating that the air tends to spread more readily toward the sidewalls, leading to a greater thickness on the outboard side (A1-1). In addition, owing to the presence of the central air barrier, which prevents the air from crossing the centerline and diffusing to the opposite side, the air-layer thickness downstream of A1-4 also remains relatively large. The resulting time-averaged mean thicknesses for A1-1 through A1-4 are 0.80, 0.76, 0.62, and 0.73 cm, respectively.

22 October 2026 13:43:54

Published under an exclusive license by AIP Publishing

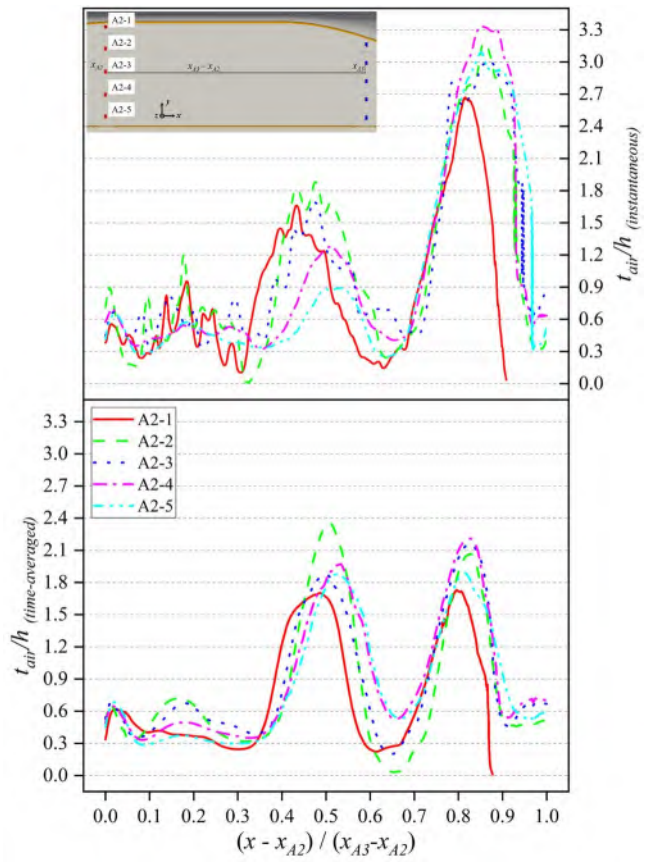

FIG. 10. Distribution of air-layer thickness t_{air} (air fraction = 0.5) between the second row of air holes (A2) and the third row (A3), instantaneous (upper), and time-averaged (lower).

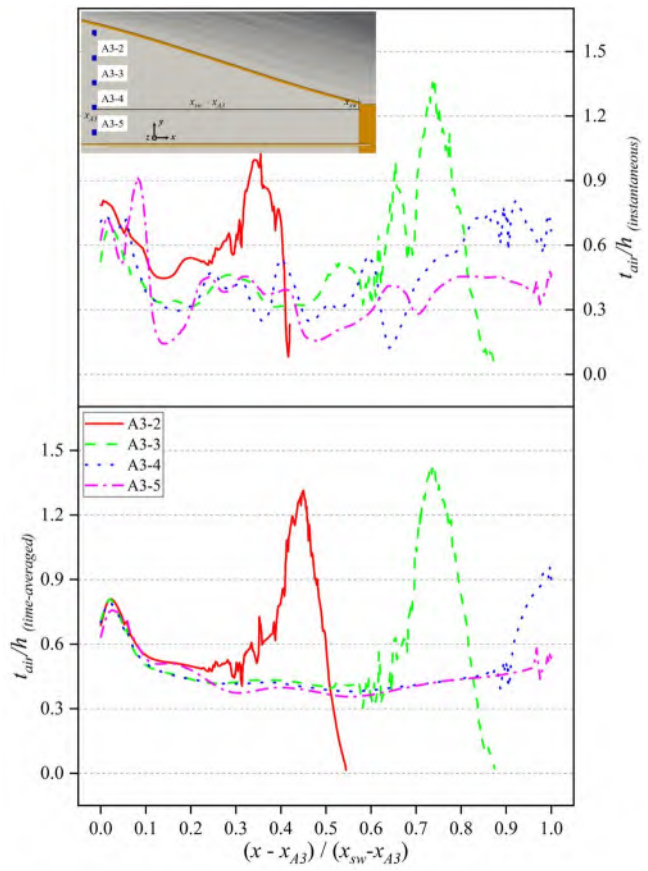

FIG. 11. Distribution of air-layer thickness t_{air} (air fraction = 0.5) between the third row of air holes (A3) and the stern wedge, instantaneous (upper), and time-averaged (lower).

Figure 10 presents the distribution of air-layer thickness in the region downstream of the second row of injection holes (A2) to the third row (A3). It can be observed that the air rapidly accumulates immediately after being injected from the holes, forming an air layer that reaches its first maximum thickness near the middle position, i.e., at $(x\text{-}x_{A2})/(x_{A3}\text{-}x_{A2}) = 0.5$. Subsequently, under the action of the outer high-speed water flow, the thickness decreases rapidly and then accumulates again, forming a second wave crest, followed by another decline in thickness. This phenomenon is consistent with the wave-like behavior of the air–water interface described above, where the interface exhibits periodic wave crests and troughs as the air layer accumulates, under the combined influence of the low-velocity inner flow and the high-velocity outer water flow.

Unlike the air-layer distribution in the bow region, the mid-ship region features a large flat bottom with parallel side barrier, and thus no spanwise contraction effect is present. Consequently, the air-layer thickness downstream of each injection hole is relatively uniform, with no significant differences among them. The air-layer thickness downstream of the second row of air holes is relatively higher, while the outermost thickness is relatively low, as a portion of the air has already begun to diffuse outboard from the ship side. The resulting time-averaged mean thicknesses for A2-1 through A2-5 are 0.76, 0.84, 0.88, 0.93, and 0.86 cm, respectively. Compared with the air-layer thickness in the bow region, a significant increase is observed, indicating that a substantial amount of air accumulates in the mid-ship region.

Figure 11 presents the distribution of air-layer thickness in the region downstream of the third row of injection holes (A3) to the stern wedge. Since the outermost air hole A3-1 is located close to the trailing edge of the ship bottom and immediately adjacent to the side air barrier, it is excluded from the analysis, and only the inner holes A3-2 through A3-5 are examined. Here, x_{sw} denotes the streamwise coordinate of the leading edge of the stern wedge.

Air-layer thickness distribution (air fraction = 0.5) between the third row of injection holes (A3) and the stern wedge, shown for instantaneous (top) and time-averaged (bottom) conditions.

It can be observed from the figure that the air flows downstream of A3-2 and A3-3 reach the side air barrier plates at $(x\text{-}x_{A3})/(x_{sw}\text{-}x_{A3}) = 0.45$ and 0.75, respectively, where the air layer is lifted due to the elevation of the wall surface. Subsequently, as the air leaves the hull and disperses, the air-layer thickness decreases rapidly. For the air flows downstream of A3-4 and A3-5, a relatively stable air-layer height can be maintained up to the leading edge of the stern wedge,

22 October 2026 13:43:54

Published under an exclusive license by AIP Publishing

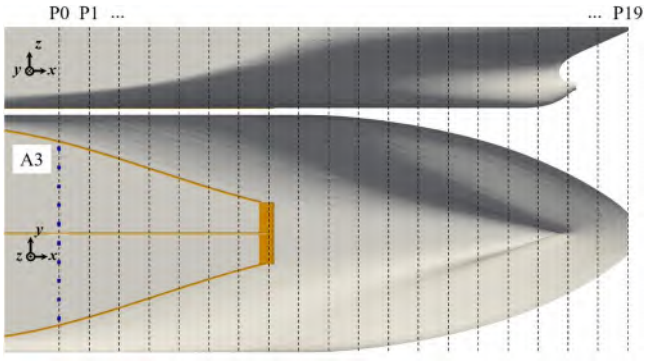

FIG. 12. Distribution of the 20 stern stations.

without exhibiting wave-like characteristics. This is attributed to the increasing flow velocity in the stern region, which prevents the air layer from developing a substantial thickness; instead, a thin air layer remains attached to the bottom wall surface until it eventually diffuses from the stern.

The resulting time-averaged mean thicknesses for A3-2 through A3-5 are 0.68, 0.61, 0.52, and 0.46 cm, respectively. Compared with the air-layer thicknesses in the upstream regions, the lowest values are observed in the stern region. This is due to two main reasons. On the one hand, a significant portion of the air has already dispersed over the side walls of the stern, resulting in a reduction in the total air volume. On the other hand, the increased flow velocity in the stern region makes it difficult for the air to accumulate and form a thick air layer.

B. Stern air-layer characteristics

For clarity, the following terminology is used throughout this section. An air layer refers to a continuous gas region beneath the hull with a phase fraction $\alpha \geq 0.5$, identified by the $\alpha = 0.5$ isosurface. A large bubble is defined as a bubble with diameter $D_b \geq 5.4$ mm or equivalently, $E_o > 4$, which tends to be significantly deformed and dominated by buoyancy and inertial effects. A microbubble is defined as a bubble with diameter $D_b \leq 1$ mm, which corresponds to the initial injected bubble size range and tends to remain nearly spherical.

At the stern, due to the contraction of the hull form and the reduction in the flat-bottomed area, the injected air escapes and disperses from the side air barrier. Under the action of buoyancy, the air rises along the side walls of the stern. At this stage, the air can generally no longer maintain a continuous air layer. Moreover, as the buoyancy direction is no longer perpendicular to the hull surface, the ascending air exhibits a discrete spatial distribution, characterized by a co-existing flow, including local air layers, large bubbles, and microbubbles. To analyze the dispersion pattern of the air at the stern, 20 cross-sectional stations were established from the third row of air hole rearward to the trailing edge of the waterline, as illustrated in Fig. 12. The streamwise positions of these stations are listed in Table III.

Based on the analysis of the mean wake fraction at the stern (Fig. 5), it is observed that the region where the wake fraction equals 0.1 is largely confined within $r/R = 1$. This radial distance also delineates the primary accumulation zone of air phase, as illustrated in Fig. 13. Consequently, for subsequent investigations into the air distribution characteristics, $r/R = 1$ is adopted as the reference radial boundary. This choice is motivated by two considerations; the first one is the contour of the wake fraction $w = 0.1$ is largely confined within this radial extent (Fig. 13), indicating that the primary region

TABLE III. The streamwise positions (x/L_{pp}) of the 20 stations located downstream of the third row of air holes at the stern.

Position	P0	P1	P2	P3	P4	P5	P6	P7	P8	P9
x/L_{pp}	0.564	0.587	0.610	0.632	0.655	0.678	0.700	0.723	0.746	0.769
Position	P10	P11	P12	P13	P14	P15	P16	P17	P18	P19
x/L_{pp}	0.791	0.814	0.837	0.859	0.882	0.905	0.928	0.950	0.973	0.996

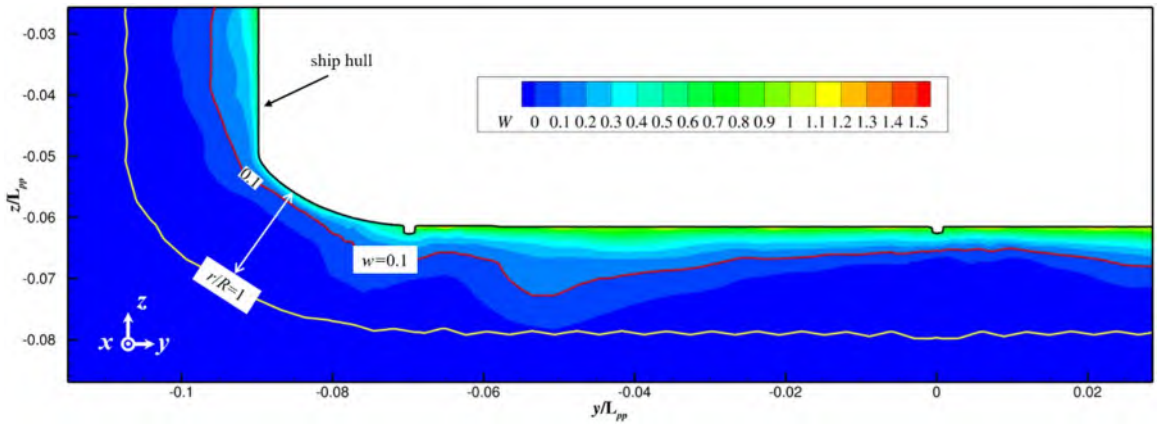

FIG. 13. The wake fraction contours on the *yz* plane at the third row of air holes ($x/L_{pp} = 0.564$).

22 October 2026 13:43:54

Published under an exclusive license by AIP Publishing

of flow deficit and air accumulation lies within $r/R = 1$; and the second one is this radius corresponds exactly to the propeller tip radius, which naturally defines the primary inflow region of the propeller disk. Since the present study focuses on the air content that may directly affect propeller performance, the analysis is deliberately restricted to this physically meaningful and geometrically well-defined region. Here, $R = 12.4$ cm denotes the propeller radius, and r/R is measured from the propeller hub. Thus, the region of interest is defined as $r/R \leq 1$, i.e., within 12.4 cm from the propeller hub, which corresponds to the propeller tip radius. This radial extent is used for the analysis of the air distribution characteristics in the present section, whereas the cylindrical domain $r/R \leq 1.2$ is used for the propeller flow field shown in Figs. 16 and 17.

Figure 14 presents the air volume fraction contours at 20 longitudinal stations along the stern. As observed, the air at the stern bottom is predominantly concentrated in the near-wall region, with markedly lower distribution in regions farther from the hull surface. On the side walls, as the buoyancy direction is not perpendicular to the wall, the air exhibits a tendency to migrate outward during upward dispersion. From the time-averaged contours, it is evident that the air diffusing from both sides is more abundant at the forward stations, while the air volume fraction at the rearward stations is comparatively lower.

Figure 15 presents the instantaneous and time-averaged air fraction distribution profiles at the 20 longitudinal stations. Both the instantaneous and time-averaged results indicate a gradual decline in air fraction with increasing distance toward the stern. At station P0, the time-averaged air fraction attains its maximum value of 4.42%,

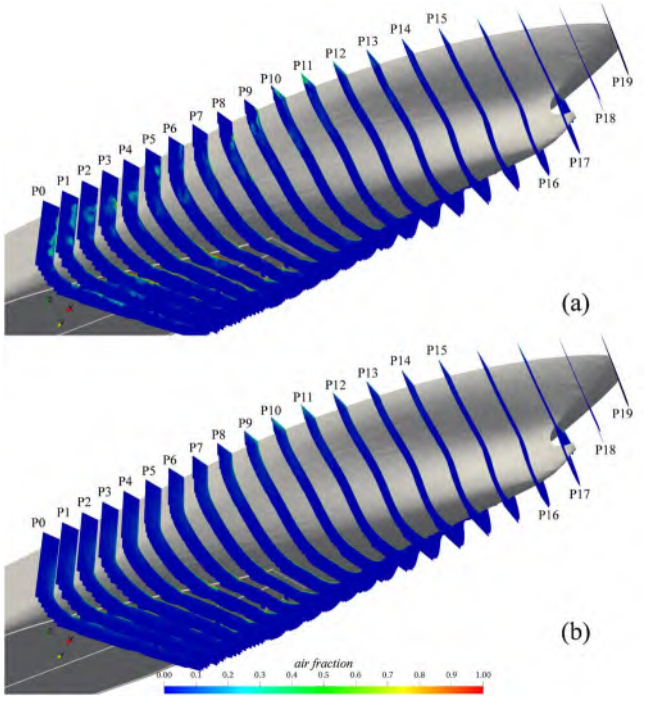

FIG. 14. Air fraction contours at 20 longitudinal stations along the stern: (a) instantaneous and (b) time-averaged.

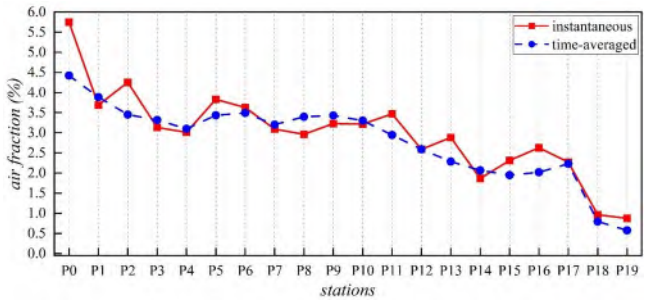

FIG. 15. The air volume fraction at 20 longitudinal stations along the stern.

whereas at stations P18 and P19, the fraction is nearly 0.57%. This trend suggests that the air continuously undergoes upward buoyancy-driven migration and lateral dispersion during its advection toward the stern. As the air progressively detaches from the near-wall region, the air volume fraction within a certain range diminishes continuously, and by the aftmost stations, the air has essentially been fully dispersed.

From the time-averaged air fraction data, a slight increase is observed between stations P4 and P7. This rise is attributable to the variation in the hull sidewall geometry within this region, where the vertical profile transitions to a curved surface. Such a geometric change reduces the upward rising velocity of the air and increases its residence time, thereby leading to transient accumulation. A similar minor increase in air volume fraction continues to appear between stations P7 and P10. In this zone, the vertical sidewall near the waterline gradually transitions toward a horizontal orientation, forming a platform-like structure that further promotes air retention.

The air-entrained wake generated by air-layer drag reduction exerts a significant influence on the stern wake field, as a portion of the entrained air may be advected into the propeller region, thereby degrading the propulsive performance of the propeller. Consequently, an investigation into the air content within the propeller flow domain is of critical importance for future assessments of the propeller performance degradation induced by the air-entrained wake in air-layer drag reduction ships.

A cylindrical region with a radius of $r/R = 1.2$, with its origin centered at the propeller hub, is delineated to represent the stern propeller flow domain, as illustrated in Fig. 16. This radial extent is larger than the $r/R \leq 1$ region used for the air distribution analysis in

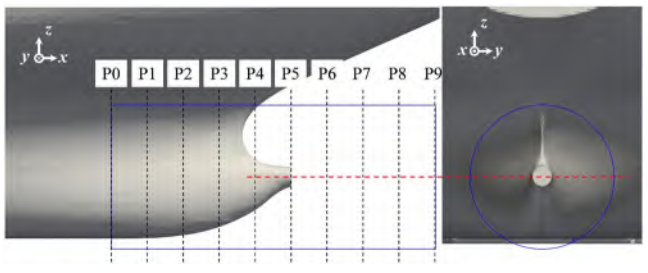

FIG. 16. Schematic diagram of the ten longitudinal stations within the propeller flow field (r/R = 1.2).

22 October 2026 13:43:54

Published under an exclusive license by AIP Publishing

TABLE IV. The streamwise positions (x/L_{pp}) of the ten stations located downstream of the propeller flow region.

Position	P0	P1	P2	P3	P4	P5	P6	P7	P8	P9
x/L_{pp}	0.911	0.921	0.931	0.941	0.951	0.961	0.970	0.980	0.990	1.000

Sec. III B, and is chosen here to fully encompass the propeller disk and its immediate inflow. Within this domain, 10 longitudinal stations were designated along the axial direction from $x/L_{pp} = 0.9114$ to 1.0 to examine the spatial variation of air content in the propeller flow field.

A cylindrical region with a radius of $r/R = 1.2$ and its origin centered at the propeller hub is delineated to represent the stern propeller flow domain, as illustrated in Fig. 16. Within this domain, ten longitudinal stations were designated along the axial direction from $x/L_{pp} = 0.9114$ to 1.0 to examine the spatial variation of air content in the propeller flow field. The locations of these stations are summarized in Table IV.

Figure 17 presents the contours of the time-averaged air fraction at ten stations behind the ship stern, within a radial range of $r/R = 1.2$. It can be observed from the figure that, for the first five stations which encompass the hull surface, the upstream air tends to flow along the wall, resulting in a relatively high air phase fraction in the near-wall region. As the station approaches the propeller hub (P5), the air fraction around the wall decreases significantly. This is primarily because most of the air has risen and dispersed due to buoyancy, with only a minor portion being carried downstream by the drag force of the water flow. When the stations are completely clear of the hull surface, a certain amount of air still remains, but the air phase fraction is markedly reduced. Based on the IATE-predicted interfacial curvature field, the computed bubble diameter $D_b = 6\alpha_a/a_i$ in this region remains within the range of approximately 0.5–1.0 mm, which falls within the microbubble definition adopted above. In this region, the air predominantly exists in the form of microbubbles, where the effect of hydrodynamic drag exceeds that of buoyancy, thereby allowing the microbubbles to be transported over a considerable distance in the streamwise direction.

The streamwise evolution of the computed bubble diameter is as follows. Within the continuous air-layer region, where the local air volume fraction is high and coalescence is active, the computed bubble diameter tends toward the upper bound of the specified range. As the air layer breaks up and the flow transitions into a dispersed air–water mixture, breakup becomes increasingly important, and the bubble diameter remains within the lower part of the specified range. In the stern wake region, where the present analysis is focused, the computed bubble diameter remains within 0.5–1.0 mm, consistent with the microbubble definition adopted in this section. This evolution is a direct consequence of the coalescence and breakup source terms in the IATE.

Figure 18 presents the contours of dimensionless water velocity (streamwise U_X/U_0 and gravitational directions U_Z/U_0, where U_0 is the freestream velocity) at stations P4 and P9. It can be observed that at the propeller hub (P4), the streamwise velocity near the wall is considerably low due to the viscous stress exerted by the wall. This low streamwise velocity facilitates the accumulation of air in the near-wall region. Meanwhile, under the influence of the separation vortex, downward velocities opposing the gravitational direction appear above and on both sides of the hub, which suppresses the upward buoyancy of the air and thereby leads to its retention within a certain range above the hub. At locations further downstream of the hub, the wake effect persists; however, the overall streamwise velocity increases substantially. Concurrently, influenced by the separation vortex, the velocity in the gravitational direction within the central region

22 October 2026 13:43:54

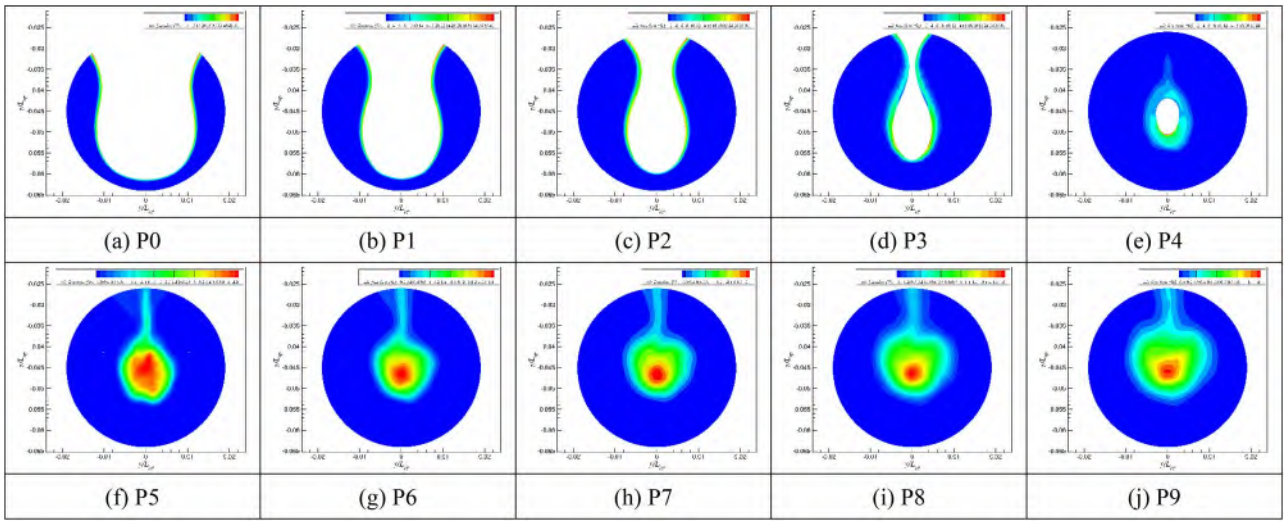

FIG. 17. Contours of the time-averaged air fraction at ten stations behind the ship stern.

Published under an exclusive license by AIP Publishing

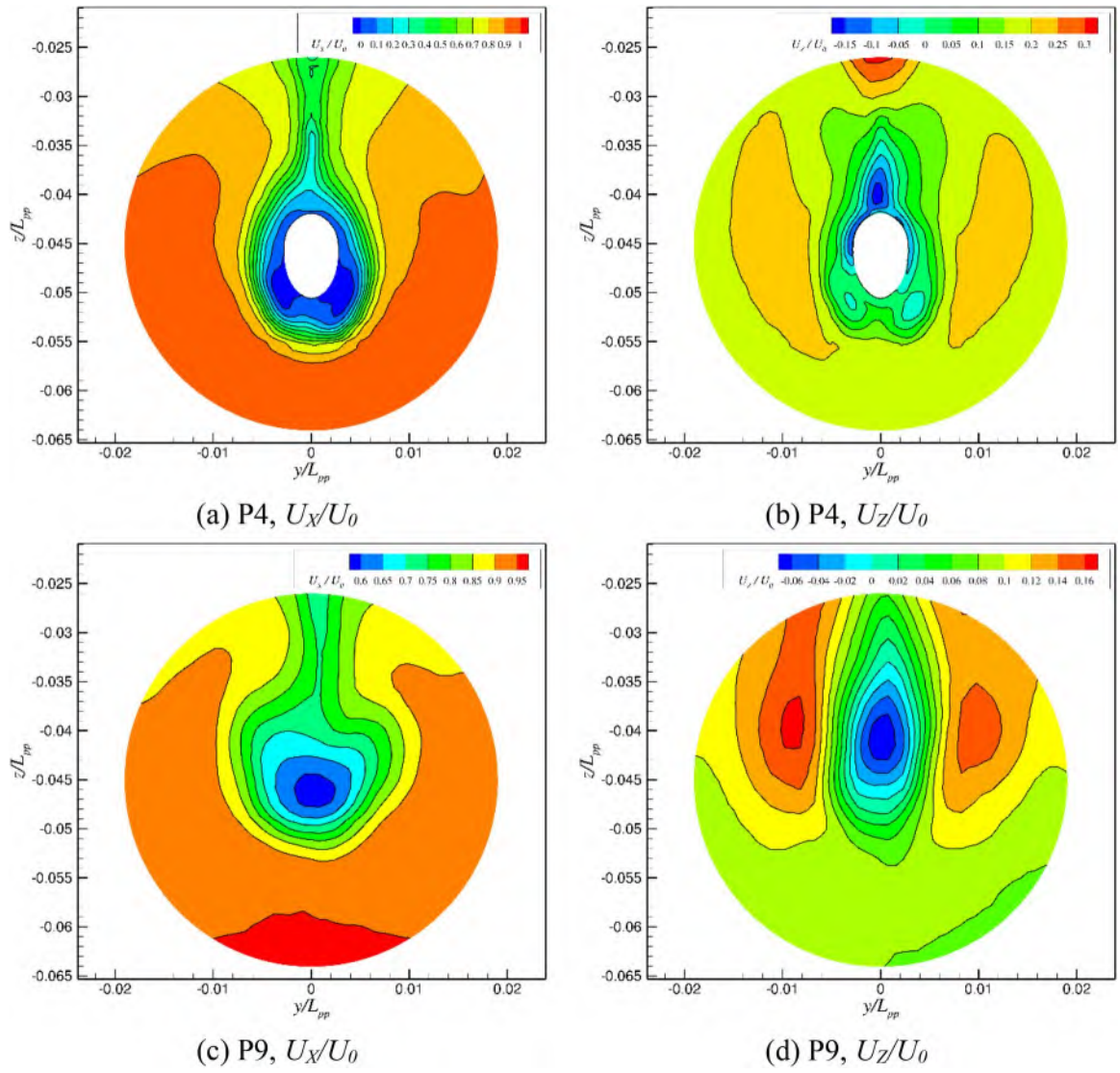

FIG. 18. Contours of dimensionless water velocity (streamwise U_X/U_0 and gravitational components U_Z/U_0) at stations P4 and P9.

remains relatively low, which continues to inhibit air buoyancy, resulting in an overall streamwise transport dominated by hydrodynamic drag. Therefore, the separation vortex at the ship stern is identified as the key factor responsible for the sustained downstream transport of dispersed air in the wake.

Figure 19 presents the air fraction results within the propeller disk plane at ten stations behind the ship stern. It can be observed that at the foremost station, the time-averaged air fraction is 2.82%. As the position moves downstream, the air fraction decreases rapidly, as the air detaches from the bottom of the propeller hub and rises due to buoyancy. Upon reaching station P5, the air has completely separated from the hull surface. At this stage, the air is transported downstream by the separated flow, and its upward buoyancy is suppressed, leading to a reduced rate of decline in the air fraction. Consequently, a relatively low air-phase fraction is maintained within a certain downstream range. Even at the rearmost station (P9), a residual air phase fraction of 0.17% is still preserved within the radial extent of the propeller disk.

It should be noted that the air fractions reported at the far downstream stations (e.g., P8 and P9 in Fig. 19) are influenced by the top symmetry boundary condition, which enforces zero normal air flux and therefore prevents air from escaping through the waterline plane, as would occur under a physical free-surface condition. Given the substantial vertical distance from the propeller disk to the top boundary and the relatively slow upward migration of air compared with the streamwise flow velocity, the effect of this boundary idealization on the near-propeller flow field is expected to be secondary. Nevertheless, the quantitative values in the far-wake region should be

22 October 2026 13:43:54

Published under an exclusive license by AIP Publishing

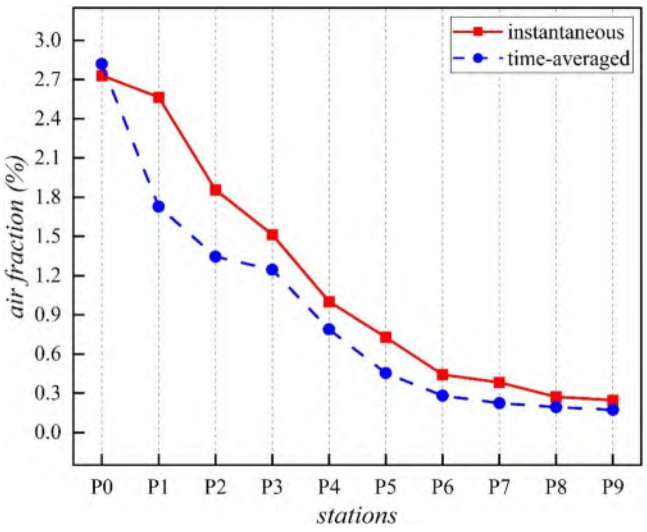

FIG. 19. Air fraction within the propeller disk plane at ten stations behind the ship stern.

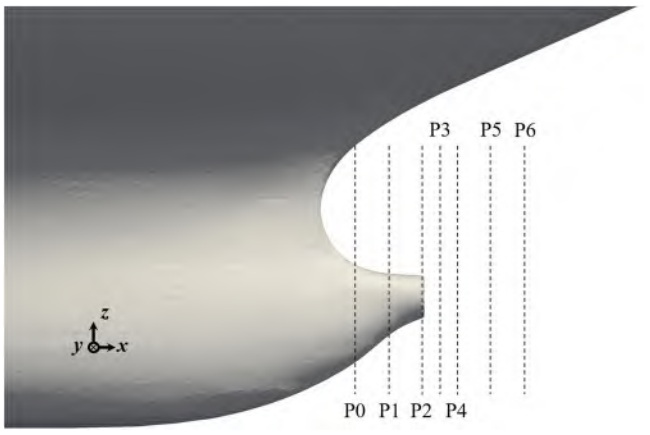

FIG. 20. Schematic diagram of the seven wake survey station locations.

TABLE V. Positions of the seven wake survey stations.

Position	P0	P1	P2	P3	P4	P5	P6
x/L_{pp}	0.944	0.950	0.956	0.959	0.961	0.967	0.973

interpreted with caution, while the overall trend of gradual air dispersion remains qualitatively valid.

C. Air–water mixed wake characteristics

The numerical simulation predicts a reduction in the mean wake fraction at the propeller disk plane of approximately 49%, compared with approximately 40% from the experiments. This overprediction of about 9 percentage points is primarily attributed to the simplifications inherent in the Euler–Euler two-fluid model with IATE closure, which introduces modeling uncertainties in the interphase interactions and near-wall two-phase dynamics. Additional factors, including grid resolution, LES with wall functions, and boundary idealizations, may also contribute to the discrepancy. Nevertheless, the numerical prediction exhibits the overall trend and the order of magnitude of the wake fraction reduction, supporting the qualitative conclusions drawn in this study.

In Sec. III B, it was demonstrated that a portion of the air generated by ALDR flows toward the ship stern, giving rise to an air-entrained wake. The air–water mixed flow further exerts a certain influence on the wake field. Accordingly, seven monitoring stations are designated to comparatively analyze the effects of the air-entrained and single-phase conditions on the stern wake, with the station layout illustrated in Fig. 20. Station P3 corresponds to the plane of the actual propeller disk. Stations P0–P2 encompass the propeller hub and a portion of the hull, while stations P4–P6 are located downstream of the propeller. The specific positions of each station are listed in Table V.

Figure 21 presents the wake fraction contours at the seven wake survey stations under single-phase and air-entrained conditions. It can be clearly observed from the results that the ALDR has a pronounced effect on the wake field. At station P0, the region of high wake fraction is more extensive under the single-phase condition, whereas under the air-entrained condition, this region is confined closely to the hull surface, forming a relatively thin high-wake-fraction zone. The same distribution pattern of wake fraction is also observed at stations P1 and P2, which encompass the propeller hub. When the stations move beyond the hull surface region, the influence of the air-entrained wake remains evident. At station P4, the high-wake-fraction region is still concentrated in the central area, with a substantially smaller extent than that under the single-phase condition. As the position moves further downstream, the flow gradually departs from the stern wall, and the overall wake fraction decreases progressively; nevertheless, the high wake fraction under the air-entrained condition remains consistently lower than that under the single-phase condition.

Overall, the air-entrained wake generated by ALDR directly affects the stern wake, resulting in a significant reduction of the high-wake-fraction region, which can persist over a considerable distance downstream of the stern. The underlying mechanisms are twofold. On the one hand, the microbubbles transported to this region by the water flow are primarily driven by hydrodynamic drag, which to some extent reduces the kinetic energy of the water and consequently leads to a decrease in local flow velocity. On the other hand, the air–water mixed flow near the wall is expected to reduce the frictional drag on the wall and to thin the boundary layer, allowing the fluid velocity to reach the freestream velocity more rapidly, which is consistent with the diminished high-wake-fraction region observed in the present simulations.

Although both mechanisms contribute to the observed wake modification, the present analysis does not quantitatively distinguish their individual contributions. Based on qualitative observations, the momentum deficit induced by microbubbles in the propeller inflow region is considered likely to play a dominant role, as it directly modifies the local velocity field, whereas the influence of wall friction reduction is considered secondary and requires further investigation.

At the actual propeller disk plane, the flow within the disk region also undergoes corresponding changes due to the influence of the air-

22 October 2026 13:43:54

Published under an exclusive license by AIP Publishing

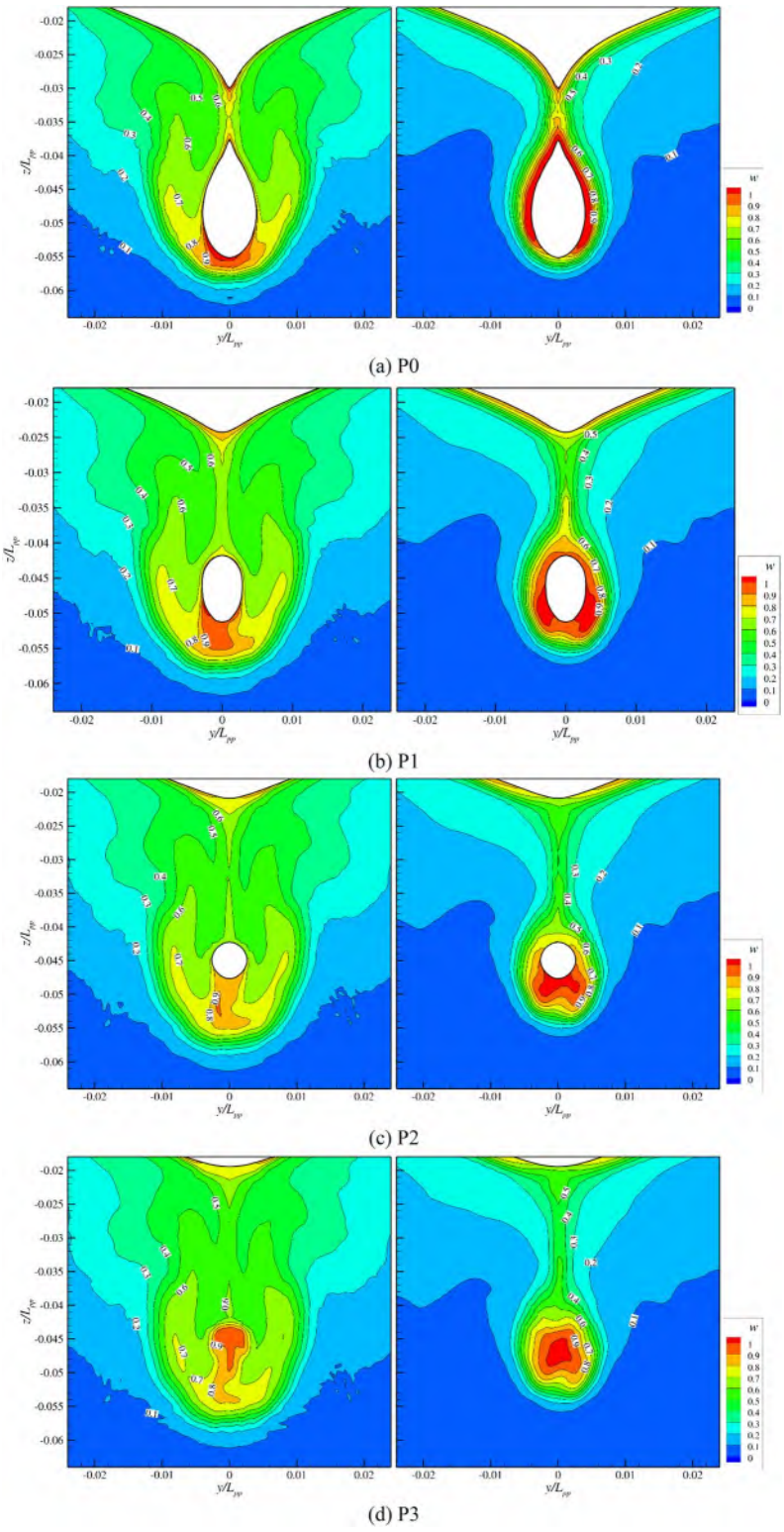

FIG. 21. Wake fraction contours at the seven stations under single-phase (left) and air-entrained (right) conditions.

22 October 2026 13:43:54

Published under an exclusive license by AIP Publishing

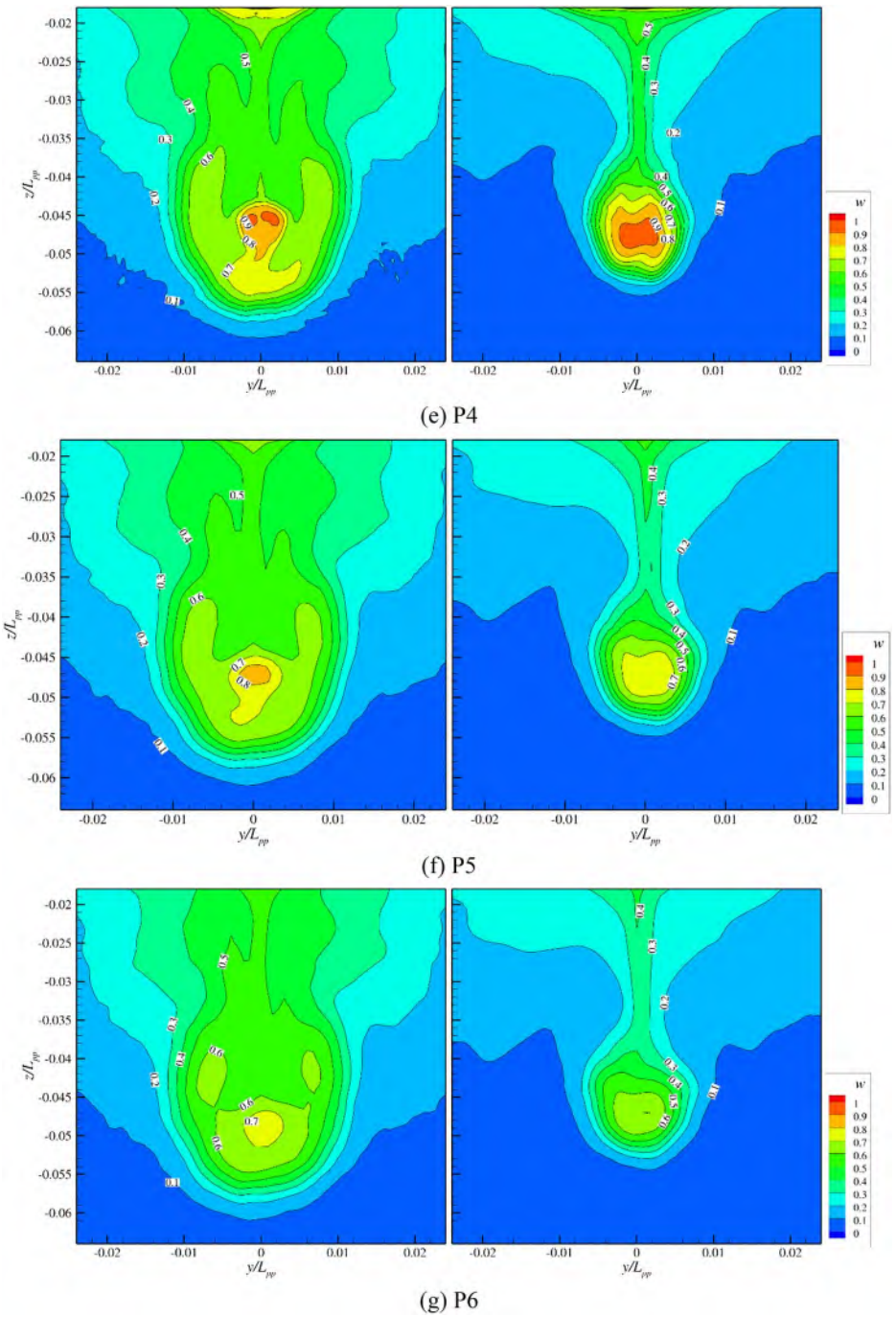

FIG. 21. (Continued.)

entrained wake generated by ALDR. Figure 22 presents the streamlines at the propeller disk plane (station P3). It can be observed from the streamline patterns that under the single-phase condition, the streamlines exhibit a pronounced dual-vortex structure, which is characteristic of the typical wake vortices of the KVLCC tanker. Under the air-entrained condition, however, the dual-vortex feature disappears and is replaced by a single-core vortex structure, with a strong axial flow present at the vortex center. The underlying mechanisms are twofold. On the one hand, the air present in the air-entrained wake modifies the original wake field structure through

22 October 2026 13:43:54

Published under an exclusive license by AIP Publishing

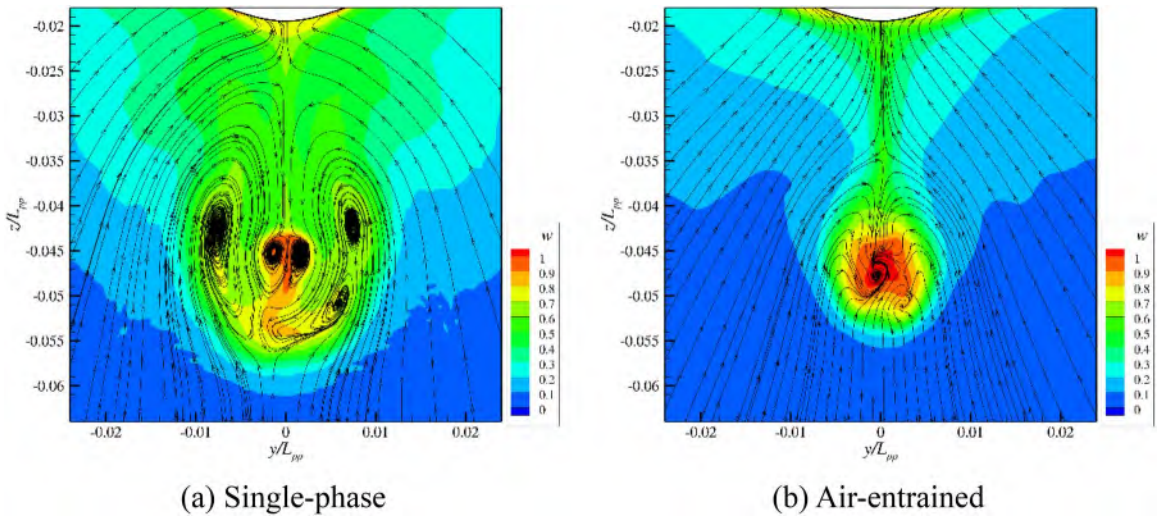

FIG. 22. Streamlines at the propeller disk plane (station P3) under single-phase and air-entrained conditions.

buoyancy effects, causing the air to converge toward the center of the flow and thereby promoting the merging of the two vortices. On the other hand, the air-layer drag reduction reduces the frictional resistance on the stern wall, alters the boundary layer velocity profile, and weakens the downward entrainment effect of the hull on the underlying water, which facilitates the mixed flow to pass through the central region and eventually form a single-vortex structure.

The transition from the dual vortex to the single-core vortex structure is correlated with air entrainment in the stern wake. Based on the observed flow features, it is plausible that buoyancy effects contribute to the convergence of air toward the center of the flow, promoting the merging of the two vortices, while the ALDR-induced reduction in wall friction and the associated modification of the boundary layer velocity profile may facilitate the mixed flow through the central region. However, we acknowledge that the present analysis does not provide a rigorous quantitative separation of these two effects, and the proposed interpretation is therefore offered as a plausible mechanism based on qualitative observations. A quantitative vorticity or momentum budget analysis is required to establish the causal decomposition and is planned for our future work.

Figure 23 presents the contours of velocity (U_X/U_0) and streamlines at the mid-longitudinal plane ($y/L_{pp} = 0$) of the ship stern. It can be observed from the streamline patterns that under the single-phase condition, the streamlines behind the propeller hub are directed vertically upward, without forming any distinct vortex structure. This corresponds to the two symmetric small vortices near the hub shown in Fig. 22(a). Since the plane is located at the symmetry plane, only upward streamlines are visible in this section. Under the air-entrained condition, however, a pronounced vortex structure appears behind the hub, corresponding to the single-core vortex in Fig. 22(b). The presence of air causes the originally symmetric vortices to merge into a single vortex, which manifests as a single-vortex structure behind the hub as the air rises away from the hub region.

A comparison of the overall streamline distributions at the stern further reveals that, under the single-phase condition, the upper streamlines are all directed downward, whereas under the air-entrained condition, they exhibit a radial spreading pattern. This is attributed to the inherent upward buoyancy tendency of the air at the stern under the air-entrained condition. The drag induced by the rising air, in turn, modifies the motion of the surrounding water, imparting a certain upward velocity component and thereby altering the streamline pattern. In addition, observation of the velocity contours at the ship bottom indicates that under the air-entrained condition, the velocity gradient is steeper, with the flow rapidly reaching the freestream velocity away from the hull surface. This is consistent with a reduction in the drag force exerted by the hull on the water under the air-entrained condition, although the present study does not quantify the wall shear stress and therefore does not provide a direct measurement of this reduction.

Finally, the scale effects of the present results should be acknowledged. The present simulations are performed at model scale ($L_{pp} = 7$ m, scale ratio 1:42), and the Reynolds number is therefore substantially lower than that of a full-scale ship. The air-layer thickness, the bubble size distribution, and the coalescence and breakup behavior of the air bubbles are all Reynolds-number dependent, and the relative importance of buoyancy and turbulent dispersion may change with scale. In particular, the IATE coefficients adopted in this study were calibrated for air–water bubbly flows at moderate Reynolds numbers, and their applicability at full scale has not been verified. Consequently, the quantitative values reported in this study, including the air-layer thickness, the air fraction at the stern, and the reduction in mean wake fraction, should be regarded as model-scale results. Extrapolation of these findings to full scale requires further study, and full-scale simulations or experiments are left for future work.

IV. CONCLUSIONS

In this study, numerical simulations are conducted on a specially designed KVLCC model-scale ship equipped with an air-layer drag reduction (ALDR) device, employing the Euler–Euler two-fluid

22 October 2026 13:43:54

Published under an exclusive license by AIP Publishing

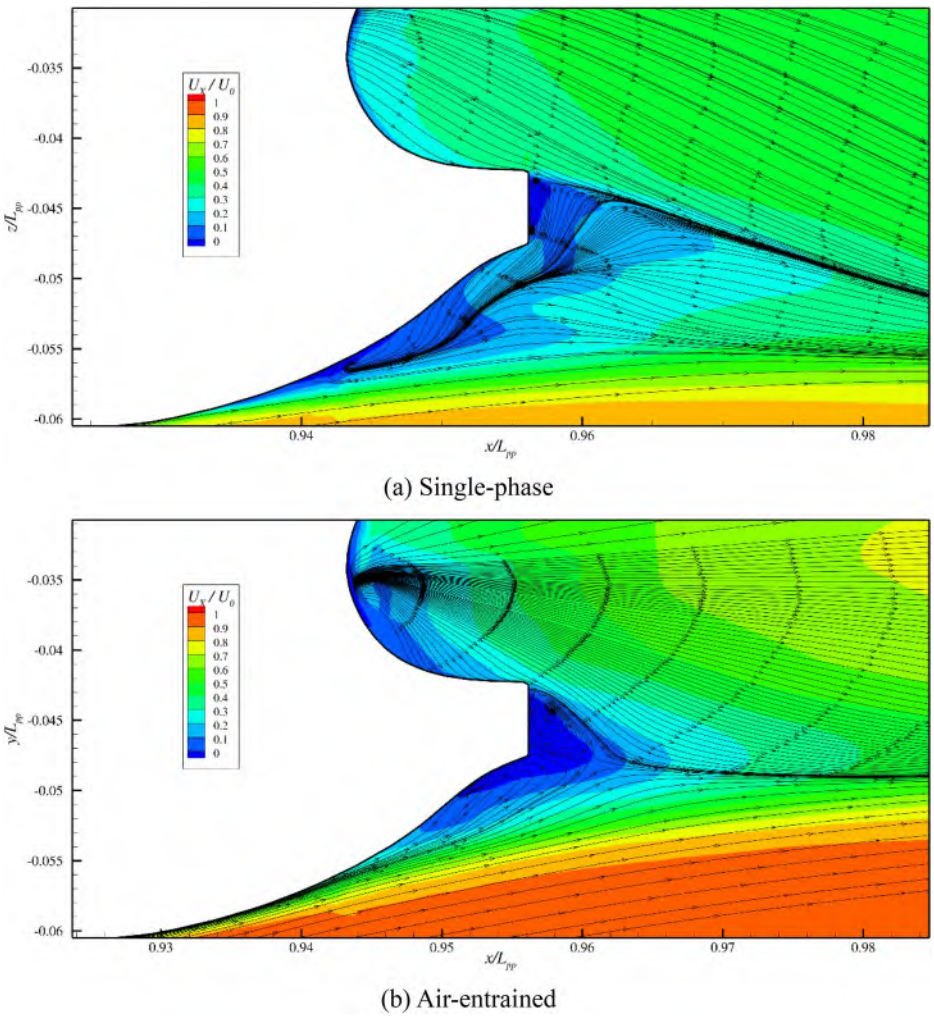

FIG. 23. Contours of normalized streamwise velocity (U_X/U_0) and streamlines at the mid-longitudinal plane ($y/L_{pp} = 0$) of the ship stern under single-phase and air-entrained conditions.

model coupled with the interfacial area transport equation (IATE). The results show that, within the present numerical framework, this method is capable of reproducing the air–water two-phase flow characteristics associated with ALDR. Through validation against experimental data, the method exhibits satisfactory accuracy in predicting the mean wake fraction at the propeller disk plane, with a relative error of approximately −9.6% under the air-entrained condition, and reasonably reproduces the spatial distribution of the air layer beneath the hull, as well as the dispersed bubble characteristics in the air-entrained stern wake. The observed transition from the dual-vortex to the single-core vortex structure at the propeller disk plane, which emerged as an additional finding of the present study, is correlated with air entrainment in the stern wake. While buoyancy and ALDR-induced boundary-layer modification are suggested as plausible contributing factors based on qualitative observations, a rigorous causal decomposition through vorticity or momentum budget analysis has not been performed and warrants further investigation. The primary contribution of this study remains the characterization of the air-layer distribution beneath the hull and the overall modifications of the stern wake field under air-entrained conditions. Based on the analysis of the air–water mixed flow around the hull, the following conclusions are drawn:

(1) The air layer beneath the hull exhibits a non-uniform distribution. Under the combined effects of the wedge-shaped structure, air injection through air holes, and lateral air barrier, the air-layer thickness displays a fluctuating pattern along the streamwise direction, characterized by a sequence of accumulation–instability–reaccumulation. The maximum time-averaged air-layer thickness (approximately 0.8–0.9 cm) is observed in the mid-ship region, whereas in the stern region, the thickness decreases markedly (to approximately 0.5–0.7 cm) due to the increased flow velocity and lateral air escape. In the stern region, the air layer becomes difficult to maintain as a continuous film and instead transitions into a dispersed flow regime comprising localized air layers, large bubbles, and microbubbles.
(2) At the ship stern, the air rises along the side walls under buoyancy and spreads outward. The air fraction decreases progressively along the streamwise direction, from 4.42% at station P0 to 0.57% at station P19. Within the propeller flow domain, a

22 October 2026 13:43:54

Published under an exclusive license by AIP Publishing

portion of the microbubbles remains constrained by the suppressing effect of the stern separation vortex, which limits their buoyant ascent and enables them to be carried by the water flow to regions far downstream of the propeller disk, with approximately 0.17% air fraction still preserved at station P9. This indicates that the separation vortex structure appears to play an important role, based on the present numerical observations, governing the sustained downstream transport of the air-entrained wake.

(3) Under the present symmetry-boundary idealization at the waterline, compared with the single-phase condition, the application of ALDR results in a notable reduction of the high-wake-fraction region in the stern, and this trend persists over a considerable distance downstream of the stern. The mean wake fraction at the propeller disk plane is reduced by approximately 49% in the present numerical simulation (compared with approximately 40% in the experiments) relative to the single-phase case, indicating a significant modification of the stern wake field under the present ALDR condition. This wake fraction reduction is associated with air entrainment in the stern region, rather than being a direct measure of drag reduction. Concurrently, the streamline pattern at the propeller disk plane transitions from the typical dual-vortex structure to a single-core vortex structure, suggesting that ALDR may modify the vorticity dynamics of the stern flow through buoyancy effects, thereby potentially affecting the uniformity of the inflow field to the propeller. It should be emphasized that this conclusion is conditional on the symmetry-boundary idealization adopted in the present study, which prevents air from escaping through the waterline; the quantitative air fraction values in the far wake should therefore be interpreted with caution. Quantitative wall friction or boundary layer modifications are not evaluated in the present study.

It should be noted that the present study primarily focuses on the feasibility and accuracy of the numerical method, with discussions centered on the air–water mixed flow and wake characteristics around the target ship model under the design speed and air injection condition. While extensive research has been devoted to air lubrication techniques for skin friction reduction, the spatial distribution of the air layer beneath the hull and the evolution of the air–water mixed wake, both of which are critical to understanding the overall drag reduction mechanism and the subsequent propeller performance, remain less explored, and these are the main concerns of the present work.

While the present numerical method has been validated against experimental wake fraction data at the propeller disk plane, the mechanistic interpretations, particularly those concerning vortex dynamics and the role of the separation vortex, are made as qualitative inferences based on the observed flow features. Systematic grid sensitivity assessments for these quantities and additional experimental validations are planned for future work. In addition, the present simulations adopt a symmetry boundary at the waterline plane, which enforces zero normal air flux and therefore retains air within the domain rather than allowing it to escape to the atmosphere. While this boundary idealization is not expected to significantly affect the near-propeller flow field due to the large vertical distance and the relatively slow buoyant rise compared with the streamwise flow, the quantitative air fraction values in the far downstream wake should still be interpreted with caution. Future studies incorporating free-surface modeling are needed to fully assess the sensitivity of the results to this boundary idealization.

In future studies, numerical simulations under a wider range of operating conditions, including varying freestream velocities, air injection rates, and the inclusion of propeller effects, will be conducted. Combined with analyses of local frictional resistance variations, a comprehensive investigation of the air–water mixed flow and drag reduction characteristics of ship ALDR will be pursued.

ACKNOWLEDGMENTS

This work was supported by the National Natural Science Foundation of China (Grant Nos. 52471335 and 52131102) and the Stabilization Support Research Project (Grant No. WDZC70202030205), to which the authors are most grateful.

AUTHOR DECLARATIONS

Conflict of Interest

The authors have no conflicts to disclose.

Author Contributions

Qidi Gao: Data curation (equal); Formal analysis (equal); Investigation (equal); Methodology (equal); Validation (equal); Visualization (equal); Writing – original draft (equal). **Xiaosong Zhang:** Conceptualization (equal); Project administration (equal); Resources (equal); Validation (equal). **Decheng Wan:** Funding acquisition (equal); Resources (equal); Software (equal); Supervision (equal). **Jianhua Wang:** Conceptualization (equal); Funding acquisition (equal); Investigation (equal); Methodology (equal); Resources (equal); Software (equal); Supervision (equal); Writing – review & editing (equal).

DATA AVAILABILITY

The data that support the findings of this study are available from the corresponding author upon reasonable request.

REFERENCES

[1]S. A. Makiharju, M. Perlin, and S. L. Ceccio, "On the energy economics of air lubrication drag reduction," Int. J. Nav. Archit. Ocean Eng. **4**(4), 412–422 (2012).
[2]E. O. Shkvar, A. S. J. E. Jamea, J. C. Cai, and A. S. Kryzhanovskyi, "Effectiveness of blowing for improving the high-speed trains aerodynamics," Thermophys. Aeromech. **25**(5), 675–686 (2018).
[3]H. Wang, K. Wang, and G. Liu, "Drag reduction by air lubrication with bubbles," Ocean Eng. **258**, 111833 (2022).
[4]S. Sindagi and R. Vijayakumar, "Succinct review of MBDR/BDR technique in reducing ship's drag," Ships Offshore Struct. **16**(9), 968–979 (2021).
[5]V. S. Lvov, A. Pomyalov, I. Procaccia, and V. Tiberkevich, "Drag reduction by microbubble in turbulent flows: The limit of minute bubbles," Phys. Rev. Lett. **94**(17), 174502 (2005).
[6]T. Takahashi, A. Kakugawa, M. Makino, and Y. Kodama, "Experimental study on scale effect of drag reduction by microbubbles using very large flat plate ships," J. Kansai Soc. Nav. Archit. **239**, 11–20 (2003).
[7]Y. Muraia, H. Fukudab, Y. Oishia, Y. Kodama, and F. Yamamoto, "Skin friction reduction by large air bubbles in a horizontal channel flow," Int. J. Multiphase Flow **33**(2), 147–163 (2007).

22 October 2026 13:43:54

Published under an exclusive license by AIP Publishing

[8]A. Kitagawa, K. Hishida, and Y. Kodama, "Two-phase turbulence structure in a microbubble channel flow," in *Proceedings of the 5th Symposium on Smart Control of Turbulence* (The University of Tokyo, 2004).
[9]Q. Gao, J. Lu, G. Zhang, J. Zhang, W. Wu, and J. Deng, "Experimental study on bubble drag reduction by the turbulence suppression in bubble flow," Ocean Eng. **272**, 113804 (2023).
[10]W. Hao, Y. Ou, and Y. Qing, "Experimental study of air layer drag reduction on a flat plate and bottom hull of a ship with cavity," Ocean Eng. **183**, 236–248 (2019).
[11]I. U. Vakarelski, A. Jetly, and S. T. Thoroddsen, "Stable-streamlined cavities following the impact of non-superhydrophobic spheres on water," Soft Matter **15**(31), 6278–6287 (2019).
[12]T. Kawamura and Y. Kodama, "Numerical simulation method to resolve interactions between bubbles and turbulence," Int. J. Heat Fluid Flow **23**(5), 627–638 (2002).
[13]A. Ferrante and S. Elghobashi, "On the physical mechanisms of drag reduction in a spatially developing turbulent boundary layer laden with microbubbles," J. Fluid Mech. **503**, 345–355 (2004).
[14]Y. M. Lau, W. Bai, N. G. Deen, and J. A. M. Kuipers, "Numerical study of bubble break-up in bubbly flows using a deterministic Euler-Lagrange framework," Chem. Eng. Sci. **108**, 9–22 (2014).
[15]R. F. Kunz, H. J. Gibeling, M. R. Maxey, G. Tryggvason, A. A. Fontaine, H. L. Petrie, and S. L. Ceccio, "Validation of two-fluid Eulerian CFD modeling for microbubble drag reduction across a wide range of Reynolds numbers," J. Fluids Eng. **129**(1), 66–79 (2007).
[16]C. Hoang, T. Yasuyuki, and S. Yugo, "A consider on drag reduction by air lubrication using integral type boundary layer computation," Jpn. Soc. Nav. Archit. Ocean Eng. **6**, 59–65 (2011).
[17]J. Xue, F. Chen, N. Yang, and W. Ge, "Eulerian–Lagrangian simulation of bubble coalescence in bubbly flow using the spring-dashpot model," Chin. J. Chem. Eng. **25**(3), 249–256 (2017).
[18]X. Zhang, J. Wang, and D. Wan, "Euler–Lagrange study of bubble drag reduction in turbulent channel flow and boundary layer flow," Phys. Fluids **32**(2), 027101 (2020).
[19]X. Zhang, J. Wang, and D. Wan, "Euler-Lagrange study of bubble breakup and coalescence in a turbulent boundary layer for bubble drag reduction," Phys. Fluids **33**(3), 037105 (2021).
[20]L. Schiller and A. A. Naumann, "A drag coefficient correlation," Z. Ver. Deutsch. Ing. **77**, 318–320 (1935).
[21]M. Ishii, "Drag coefficient and relative velocity in bubbly, droplet or particulate flows," AlChE J. **25**(5), 843–855 (1979).
[22]A. Tomiyama, H. Tamai, I. Zun *et al.*, "Transverse migration of single bubbles in simple shear flows," Chem. Eng. Sci. **57**(11), 1849–1858 (2002).
[23]M. Ishii and K. Mishima, "Two-fluid model and hydrodynamic constitutive relation," Nucl. Eng. Des. **82**(2), 107–126 (1984).
[24]X. Zhao and Z. Zong, "Experimental and numerical studies on the air-injection drag reduction of the ship model," Ocean Eng. **251**, 111032 (2022).
[25]X. Shao, N. Liang, S. Qin, L. Cao, and D. Wu, "Numerical investigation of microbubble drag reduction on an axisymmetric body based on Eulerian multiphase model," Ocean Eng. **298**, 117157 (2024).
[26]J. Mohammadpour, F. Salehi, V. Garaniya *et al.*, "Computational analysis of air bubble-induced frictional drag reduction on ship hulls," J. Mar. Sci. Technol. **29**(3), 696–710 (2024).
[27]X. Zhao, Y. Hao, J. Cui *et al.*, "Numerical investigations on drag reduction by micro-bubbles of KVLCC2 ship model by means of OpenFOAM," Ocean Eng. **341**, 122609 (2025).
[28]Q. Gao, W. Wang, J. Wang, and D. C. Wan, "Numerical simulation of air-liquid two-phase flow in air-layer drag reduction ship utilizing the Euler-Euler method," in *ISOPE International Ocean and Polar Engineering Conference* (ISOPE, 2025), p. ISOPE-1.
[29]Z. Wang, J. Gu, and H. Qian, "The impact of actively injecting bubbles on propeller performance," Ocean Eng. **333**, 121518 (2025).
[30]D. A. Drew and R. T. Lahey, Jr., "Application of general constitutive principles to the derivation of multidimensional two-phase flow equations," Int. J. Multiphase Flow **5**(4), 243–264 (1979).
[31]A. D. Burns *et al.*, "The Favre averaged drag model for turbulent dispersion in Eulerian multi-phase flows," in *5th International Conference on Multiphase Flow* (ICMF, 2004).
[32]S. P. Antal, R. T. Lahey, Jr., and J. E. Flaherty, "Analysis of phase distribution in fully developed laminar bubbly two-phase flow," Int. J. Multiphase Flow **17**(5), 635–652 (1991).
[33]J. Smagorinsky, "General circulation experiments with the primitive equations: I. The basic experiment," Mon. Weather Rev. **91**(3), 99–164 (1963).
[34]P. E. Turkeltaub, D. L. Flowers, L. G. Lyon, and G. F. Eden, "Development of ventral stream representations for single letters," Ann. N. Y. Acad. Sci. **1145**(1), 13–29 (2008).
[35]M. Ishii, S. Kim, and J. Uhle, "Interfacial area transport equation: Model development and benchmark experiments," Int. J. Heat Mass Transfer **45**(15), 3111–3123 (2002).
[36]Q. Gao, X. Zhang, J. Wang, and D. Wan, "Study on the characteristics of air layer for air layer drag reduction over a 2D flat plate based on the Euler-Euler method," in *ISOPE International Ocean and Polar Engineering Conference* (ISOPE, 2026), p. ISOPE-1.
[37]J. W. Miles, "On the generation of surface waves by shear flows," J. Fluid Mech. **3**(2), 185–204 (1957).
[38]S. A. Thorpe, "On the shape of progressive internal waves," Philos. Trans. R. Soc., A **263**(1145), 563–614 (1968).
[39]M. L. Banner and D. H. Peregrine, "Wave breaking in deep water," Annu. Rev. Fluid Mech. **25**, 373–397 (1993).
[40]J. H. Duncan, "Spilling breakers," Annu. Rev. Fluid Mech. **33**, 519–547 (2001).

22 October 2026 13:43:54

Published under an exclusive license by AIP Publishing